

---

# CMS Physics Analysis Summary

---

Contact: cms-pag-conveners-higgs@cern.ch

2019/03/22

## Measurements of properties of the Higgs boson in the four-lepton final state in proton-proton collisions at $\sqrt{s} = 13$ TeV

The CMS Collaboration

### Abstract

Properties of the Higgs (H) boson are measured in the  $H \rightarrow ZZ \rightarrow 4\ell$  ( $\ell = e, \mu$ ) decay channel. The full data sample of proton-proton collisions at a center-of-mass energy of 13 TeV is used, corresponding to an integrated luminosity of  $137.1 \text{ fb}^{-1}$  recorded in 2016, 2017, and 2018 by the CMS detector at the LHC. The signal-strength modifier  $\mu$ , defined as the ratio of the H boson rate in the  $4\ell$  channel to the Standard Model (SM) expectation, is measured to be  $\mu = 0.94^{+0.07}_{-0.07}(\text{stat.})^{+0.08}_{-0.07}(\text{syst.})$  with the H boson mass profiled in the fit. The signal-strength modifiers for different H boson production modes are also constrained. Measurements of the simplified template cross sections, designed to quantify the different H boson production processes in specific regions of phase space, are reported. The cross section for the production of the  $H \rightarrow 4\ell$  in a fiducial region closely matching the experimental selection of the leptons is measured to be  $\sigma_{\text{fid.}} = 2.73^{+0.23}_{-0.22}(\text{stat.})^{+0.24}_{-0.19}(\text{syst.}) \text{ fb}$  at  $m_H = 125.09 \text{ GeV}$ , compared to a SM prediction of  $2.76 \pm 0.14 \text{ fb}$ . Differential cross sections as a function of the  $p_T$  and rapidity of the H boson, the number of associated jets, and the  $p_T$  of the leading associated jet are determined. All results are found to be compatible with the SM predictions, within the measurements precision.



## 1 Introduction

The ATLAS and CMS Collaborations first reported the discovery of a new particle in 2012 [1, 2] consistent with the Standard Model (SM) Higgs (H) boson [3–8]. Subsequent studies by CMS using the full LHC Run 1 data in various decay channels and production modes, combined measurements from ATLAS and CMS as well as combination of the CMS results with Run 2 data from 2016 and 2017 [9–15] showed that the properties of the new boson are so far consistent with expectations for the SM H boson.

The  $H \rightarrow ZZ \rightarrow 4\ell$  decay channel ( $\ell = e, \mu$ ) has a large signal-to-background ratio due to the complete reconstruction of the final state decay products and excellent lepton momentum resolution. This makes it a most important channel for studies of the H boson’s properties. Measurements performed using this decay channel with the Run 1 and Run 2 data set include the determination of the mass and spin-parity of the new boson [16–18], its width [19, 20], fiducial cross sections [14, 21], and the tensor structure of its interaction with a pair of neutral gauge bosons in both on-shell and off-shell regions [18, 20, 22, 23].

The measurements of the properties of the H boson in the  $H \rightarrow ZZ \rightarrow 4\ell$  decay channel in proton-proton (pp) collisions at  $\sqrt{s} = 13$  TeV are reported for a combined  $137.1 \text{ fb}^{-1}$  of data collected in 2016, 2017, and 2018. In the following, the techniques used to analyze the data collected in 2018 ( $59.7 \text{ fb}^{-1}$ ) with the CMS detector are described. Measurement of the inclusive and differential cross-sections in a fiducial region closely matching the experimental selection are presented, together with the first measurement of the so-called Stage 1.1 of the Simplified Template Cross-Sections (STXS) approach [24, 25]. The analysis for previously published results using 2016 [14] and 2017 [15] data remain unchanged except for a new categorization of the selected events to improve the sensitivity to the STXS.

## 2 The CMS detector

The central feature of the CMS apparatus is a superconducting solenoid of 6 m internal diameter, providing a magnetic field of 3.8 T. Within the solenoid volume are a silicon pixel and strip tracker, a lead tungstate crystal electromagnetic calorimeter (ECAL), and a brass and scintillator hadron calorimeter (HCAL), each composed of a barrel and two endcap sections. An entirely new pixel detector has been installed in 2017, featuring a full silicon device with 4 layers in the barrel and 3 disks in the endcaps [26], providing a four hits coverage system and reduced material budget in front of the calorimeters. Forward calorimeters extend the pseudorapidity ( $\eta$ ) coverage provided by the barrel and endcap detectors. Muons are measured in gas-ionization detectors embedded in the steel flux-return yoke outside the solenoid. A more detailed description of the CMS detector, together with a definition of the coordinate system used and the relevant kinematic variables, can be found in Ref. [27].

## 3 Data and simulated samples

This analysis makes use of pp collision data recorded in 2016, 2017, and 2018 by the CMS detector corresponding to an integrated luminosity of  $137.1 \text{ fb}^{-1}$ . For the year 2018, it corresponds to  $59.7 \text{ fb}^{-1}$ , where collision events are selected by high-level trigger algorithms that require the presence of leptons passing loose identification and isolation requirements. The main triggers of the 2018 analysis select either a pair of electrons or muons, or an electron and a muon. The minimal transverse momentum of the leading electron (muon) is 23 (17) GeV, while that of the subleading lepton is 12 (8) GeV. To maximize the coverage of the  $H \rightarrow 4\ell$  phase space, triggers

requiring three leptons with relaxed  $p_T$  thresholds and no isolation requirement are also used, as are isolated single-electron and single-muon triggers with thresholds of 32 GeV and 24 GeV, respectively. The overall trigger efficiency for simulated signal events that pass the full selection chain of this analysis is larger than 99%. The trigger efficiency is measured in data using a sample of  $4\ell$  events collected by the single-lepton triggers and is found to be in agreement with the expectation from simulation.

Monte Carlo (MC) simulation samples for the signals and the relevant background processes are used to estimate backgrounds, optimize the event selection, and evaluate the acceptance and systematic uncertainties. The SM H boson signals are generated at next-to-leading order (NLO) in perturbative QCD (pQCD) with the POWHEG 2.0 [28–30] generator for the five main production processes: gluon fusion (ggH), vector boson fusion (VBF) and associated production (WH, ZH and t $\bar{t}$ H). For VH (V = W or Z) the MINLO HVJ [31] extension of POWHEG 2.0 is used. The cross section for the dominant ggH production mode is taken from Ref. [32]. Two other production modes, b $\bar{b}$ H and tH, are generated using JHUGEN [33–36]. In all cases, the decay of the H boson to four leptons is modeled with JHUGEN [33, 34].

The SM ZZ background contribution from quark-antiquark annihilation is generated at NLO pQCD with POWHEG 2.0, while the gg  $\rightarrow$  ZZ process is generated at leading order (LO) with MCFM [37]. Reducible background is estimated from data as described in section 7.2.

The default parton distribution functions (PDF) used are NNPDF31\_nlo\_hessian\_pdfas and NNPDF31\_lo\_as\_0130 [38] for NLO and LO simulations, respectively. All signal and background event generators are interfaced with PYTHIA 8 [39] tune CUETP8M1 [40] to simulate the multi-parton interaction and hadronization effects. The generated events are processed through a detailed simulation of the CMS detector based on GEANT4 [41, 42] and are reconstructed with the same algorithms that are used for data. The simulated events include overlapping pp interactions (pileup) and have been reweighted so that the distribution of the number of interactions per LHC bunch crossing in simulation matches that observed in data.

## 4 Event reconstruction and selection

The particle-flow algorithm [43] aims to reconstruct and identify each individual particle in an event, with an optimized combination of information from the various elements of the CMS detector. The energy of photons is directly obtained from the ECAL measurement, corrected for zero-suppression effects. The reconstructed vertex with the largest value of summed physics-object  $p_T^2$  is taken to be the primary pp interaction vertex.

The energy of electrons is determined from a combination of the electron momentum at the primary interaction vertex as determined by the tracker, the energy of the corresponding ECAL cluster, and the energy sum of all bremsstrahlung photons spatially compatible with originating from the electron track. The energy of muons is obtained from the curvature of the corresponding track. The energy of charged hadrons is determined from a combination of their momentum measured in the tracker and the matching ECAL and HCAL energy deposits, corrected for zero-suppression effects and for the response function of the calorimeters to hadronic showers. Finally, the energy of neutral hadrons is obtained from the corresponding corrected ECAL and HCAL energy.

Muons within the geometrical acceptance  $|\eta^\mu| < 2.4$  and  $p_T^\mu > 5$  GeV are reconstructed by combining information from the silicon tracker and the muon system [44]. The matching between the inner and outer tracks proceeds either outside-in, starting from a track in the muon sys-

tem, or inside-out, starting from a track in the silicon tracker. Tracker tracks that match track segments in only one or two stations of the muon system are also considered in the analysis to collect very low- $p_T$  muons that may not have sufficient energy to penetrate the entire muon system. The muons are selected among the reconstructed muon track candidates by applying minimal requirements on the track in both the muon system and inner tracker system, and taking into account compatibility with small energy deposits in the calorimeters.

To discriminate between prompt muons from  $Z$  boson decay and those arising from electroweak decays of hadrons within jets, an isolation requirement of  $\mathcal{I}^\mu < 0.35$  is imposed, where the relative isolation is defined as

$$\mathcal{I}^\mu \equiv \left( \sum p_T^{\text{charged}} + \max [0, \sum p_T^{\text{neutral}} + \sum p_T^\gamma - p_T^{\text{PU}}(\mu)] \right) / p_T^\mu. \quad (1)$$

In Eq. 1,  $\sum p_T^{\text{charged}}$  is the scalar sum of the transverse momenta of charged hadrons originating from the chosen primary vertex of the event. The  $\sum p_T^{\text{neutral}}$  and  $\sum p_T^\gamma$  are the scalar sums of the transverse momenta for neutral hadrons and photons, respectively. Since the isolation variable is particularly sensitive to undesirable energy deposits from pileup interactions, a  $p_T^{\text{PU}}(\mu)$  contribution is subtracted. We define  $p_T^{\text{PU}}(\mu) \equiv 0.5 \sum_i p_T^{\text{PU},i}$  where  $i$  runs over the momenta of the charged hadron PF candidates not originating from the primary vertex, and the factor of 0.5 corrects for the different fraction of charged and neutral particles in the cone. The isolation sums involved are all restricted to a volume bounded by a cone of angular radius  $\Delta R = 0.3$  around the muon direction at the primary vertex, where the angular distance between two particles  $i$  and  $j$  is  $\Delta R(i, j) = \sqrt{(\eta^i - \eta^j)^2 + (\phi^i - \phi^j)^2}$ .

An algorithm is used to collect the final-state radiation (FSR) of leptons. Photons which are selected are excluded from the isolation computation of selected muons in the event.

Electrons are reconstructed within the geometrical acceptance defined by pseudorapidity  $|\eta^e| < 2.5$  and for transverse momentum  $p_T^e > 7 \text{ GeV}$  with an algorithm that combines information from the ECAL and the tracker [45]. Electrons are identified using a multivariate discriminant which includes observables sensitive to the presence of bremsstrahlung along the electron trajectory, the geometrical and momentum-energy matching between the electron trajectory and the associated cluster in the ECAL, the shape of the electromagnetic shower in the ECAL, and variables that discriminate against electrons originating from photon conversions. Discriminant also includes the isolation sums described above ( $\sum p_T^{\text{charged}}$ ,  $\sum p_T^{\text{neutral}}$ , and  $\sum p_T^\gamma$ ) but computed around the electron direction. The inclusion of isolation sums helps suppressing electrons originating from electroweak decays of hadrons within jets [46].

The package `xgboost` [47] is used for the training and optimization of the multivariate discriminant employed for electron identification and isolation. They are performed using simulation and are divided into six regions formed from two transverse momentum ranges (7–10 GeV and  $>10 \text{ GeV}$ ) and three pseudorapidity regions: central barrel ( $|\eta^e| < 0.8$ ), outer barrel ( $0.8 < |\eta^e| < 1.479$ ), and endcaps ( $1.479 < |\eta^e| < 2.5$ ).

In order to suppress muons originating from in-flight decays of hadrons and electrons from photon conversions, we require each lepton track to have a 3D impact parameter significance with respect to the primary vertex less than 4.

The momentum scale and resolution of electrons and muons are calibrated in bins of  $p_T^\ell$  and  $\eta^\ell$  using the decay products of known dilepton resonances. The lepton momentum scale in data is corrected with a  $Z \rightarrow \ell^+ \ell^-$  sample, by matching the peak of the reconstructed dilepton mass spectrum to the known value of  $m_Z$ , and a pseudorandom Gaussian smearing is applied to

lepton energies in simulation to make the  $Z \rightarrow \ell^+ \ell^-$  mass resolution in simulation match the one in data.

A “tag and probe” technique using samples of Z boson events in data and simulation is used to measure the efficiency of the reconstruction and selection for prompt electrons and muons in several bins of  $p_T^\ell$  and  $\eta^\ell$ . The difference in the efficiencies measured in simulation and data is used to rescale the yields of selected events in the simulated samples.

For each event, hadronic jets are clustered from the reconstructed particles using the infrared and collinear safe anti- $k_T$  algorithm [48, 49] with a distance parameter of 0.4. The jet momentum is determined as the vectorial sum of all particle momenta in the jet, and is found from simulation to be within 5 to 10% of the true momentum over the whole  $p_T$  spectrum and detector acceptance. Additional proton-proton interactions within the same or nearby bunch crossings can contribute additional tracks and calorimetric energy depositions to the jet momentum. To mitigate this effect, tracks identified to be originating from pileup vertices are discarded and an offset correction is applied to correct for remaining contributions. Jet energy corrections are derived from simulation to bring measured response of jets to that of particle level jets on an average. In situ measurements of the momentum balance in dijet, photon + jet, Z + jet, and multijet events are used to account for any residual differences in jet energy scale in data and simulation [50]. The jet energy resolution amounts typically to 16% at 30 GeV, 8% at 100 GeV, and 4% at 1 TeV. Additional selection criteria are applied to each jet to remove jets potentially dominated by anomalous contributions from various subdetector components or reconstruction failures. To be considered in the analysis, jets must satisfy  $p_T^{\text{jet}} > 30$  GeV and  $|\eta^{\text{jet}}| < 4.7$ , and be separated from all selected lepton candidates and any selected FSR photons by  $\Delta R(\ell/\gamma, \text{jet}) > 0.4$ . Jets are also required to pass tight identification criteria with efficiency  $> 99\%$  and to pass tight working point of pileup jet identification [51].

For event categorization, jets are tagged as b-jets using the DeepCSV algorithm [52] which, in particular, combines information about impact parameter significance, the secondary vertex, and jet kinematics. Data to simulation scale factors for the b-tagging efficiency are applied as a function of jet  $p_T$ ,  $\eta$  and flavor.

The event selection is designed to extract signal candidates from events containing at least four well-identified and isolated leptons, each originating from the primary vertex and possibly accompanied by an FSR photon candidate. In what follows, unless otherwise stated, FSR photons are included in invariant mass computations.

First, Z candidates are formed with pairs of leptons of the same flavor and opposite-charge ( $e^+e^-$ ,  $\mu^+\mu^-$ ) and required to pass  $12 < m_{\ell^+\ell^-} < 120$  GeV. They are then combined into ZZ candidates, wherein we denote as  $Z_1$  the Z candidate with an invariant mass closest to the nominal Z boson mass [53], and as  $Z_2$  the other one. The flavors of involved leptons define three mutually exclusive subchannels:  $4e$ ,  $4\mu$  and  $2e2\mu$ .

To be considered for the analysis, ZZ candidates have to pass a set of kinematic requirements that improve the sensitivity to Higgs boson decays. The  $Z_1$  invariant mass must be larger than 40 GeV. All leptons must be separated in angular space by at least  $\Delta R(\ell_i, \ell_j) > 0.02$ . At least two leptons are required to have  $p_T > 10$  GeV and at least one is required to have  $p_T > 20$  GeV. In the  $4\mu$  and  $4e$  subchannels, where an alternative  $Z_a Z_b$  candidate can be built out of the same four leptons, we discard candidates with  $m_{Z_b} < 12$  GeV if  $Z_a$  is closer to the nominal Z boson mass than  $Z_1$  is. This protects against events that contain an on-shell Z and a low-mass dilepton resonance. To further suppress events with leptons originating from hadron decays in jet fragmentation or from the decay of low-mass resonances, all four opposite-

charge lepton pairs that can be built with the four leptons (irrespective of flavor) are required to satisfy  $m_{\ell^+\ell^-} > 4$  GeV, where selected FSR photons are disregarded in the invariant mass computation. Finally, the four-lepton invariant mass  $m_{4\ell}$  must be larger than 70 GeV, which defines the mass range of interest for the subsequent steps of the analysis.

In events where more than one ZZ candidate passes the above selection, the candidate with the highest value of  $\mathcal{D}_{\text{bkg}}^{\text{kin}}$  (defined in Section 5) is retained, except if two candidates consist of the same four leptons in which case the candidate with the  $Z_1$  mass closest to the nominal Z boson mass is retained.

## 5 Kinematic discriminants

The full kinematic information from each event using either the H boson decay products or associated particles in its production is extracted using matrix element calculations and used to form several kinematic discriminants. These computations rely on the MELA package [1, 33–35] and use JHUGEN matrix elements for the signal and MCFM matrix elements for the background. Both H boson decay kinematics and kinematics of associated production of H+jet, H+2 jets, VBF, ZH, WH are explored in this analysis. The full event kinematics is described by decay observables  $\vec{\Omega}^{\text{H} \rightarrow 4\ell}$  or observables describing associated production  $\vec{\Omega}^{\text{H}+\text{JJ}}$ .

The discriminant sensitive to the  $gg/q\bar{q} \rightarrow 4\ell$  kinematics is calculated as [1, 18]

$$\mathcal{D}_{\text{bkg}}^{\text{kin}} = \left[ 1 + \frac{\mathcal{P}_{\text{bkg}}^{\text{q}\bar{\text{q}}}(\vec{\Omega}^{\text{H} \rightarrow 4\ell} | m_{4\ell})}{\mathcal{P}_{\text{sig}}^{\text{gg}}(\vec{\Omega}^{\text{H} \rightarrow 4\ell} | m_{4\ell})} \right]^{-1}, \quad (2)$$

where  $\mathcal{P}_{\text{sig}}^{\text{gg}}$  is the probability for the signal and  $\mathcal{P}_{\text{bkg}}^{\text{q}\bar{\text{q}}}$  is the probability for the dominant  $q\bar{q} \rightarrow 4\ell$  background process, all calculated within the MELA framework.

In VBF and VH-hadronic categories, the contamination from ggH is significant. Therefore, dedicated production-dependent  $\mathcal{D}_{\text{bkg}}$  discriminants used in the VBF-2jet-tagged and VH-hadronic-tagged categories and all their sub-categories are defined as:

$$\begin{aligned} \mathcal{D}_{\text{bkg}}^{\text{VBF+dec}} &= \frac{\mathcal{P}_{\text{sig}}^{\text{VBF+VH+dec}}(\vec{\Omega})}{\mathcal{P}_{\text{sig}}^{\text{VBF+VH+dec}}(\vec{\Omega}) + c^{\text{VBF2jet}}(m_{4\ell}) \times (\mathcal{P}_{\text{bkg}}^{\text{VBS+VVV}}(\vec{\Omega}) + \mathcal{P}_{\text{bkg}}^{\text{QCD+dec}}(\vec{\Omega}))} \\ \mathcal{D}_{\text{bkg}}^{\text{VH+dec}} &= \frac{\mathcal{P}_{\text{sig}}^{\text{VBF+VH+dec}}(\vec{\Omega})}{\mathcal{P}_{\text{sig}}^{\text{VBF+VH+dec}}(\vec{\Omega}) + c^{\text{had.VH}}(m_{4\ell}) \times (\mathcal{P}_{\text{bkg}}^{\text{VBS+VVV}}(\vec{\Omega}) + \mathcal{P}_{\text{bkg}}^{\text{QCD+dec}}(\vec{\Omega}))}, \end{aligned} \quad (3)$$

where  $\mathcal{P}_{\text{sig}}^{\text{VBF+VH+dec}}$  is the probability for VBF and VH signal,  $\mathcal{P}_{\text{bkg}}^{\text{VBS+VVV}}$  is the probability for vector boson scattering and tri-boson background,  $\mathcal{P}_{\text{bkg}}^{\text{QCD+dec}}$  is the probability for QCD production and  $c^p(m_{4\ell})$  for category  $p$  is the  $m_{4\ell}$ -dependent constant to calibrate the distribution.

Four discriminants calculated following prescription in Ref. [20, 54] are used to enhance the purity of event categories as described in Section 6. The discriminant sensitive to the VBF signal topology with two associated jets, the VBF signal topology with one associated jet, and

to the VH (either ZH or WH) signal topology with two associated jets are

$$\begin{aligned} \mathcal{D}_{2\text{jet}} &= \left[ 1 + \frac{\mathcal{P}_{\text{HJJ}}(\vec{\Omega}^{\text{H+JJ}}|m_{4\ell})}{\mathcal{P}_{\text{VBF}}(\vec{\Omega}^{\text{H+JJ}}|m_{4\ell})} \right]^{-1} & \mathcal{D}_{1\text{jet}} &= \left[ 1 + \frac{\mathcal{P}_{\text{HJ}}(\vec{\Omega}^{\text{H+J}}|m_{4\ell})}{\int d\eta_j \mathcal{P}_{\text{VBF}}(\vec{\Omega}^{\text{H+JJ}}|m_{4\ell})} \right]^{-1} \\ \mathcal{D}_{\text{WH}} &= \left[ 1 + \frac{\mathcal{P}_{\text{HJJ}}(\vec{\Omega}^{\text{H+JJ}}|m_{4\ell})}{\mathcal{P}_{\text{WH}}(\vec{\Omega}^{\text{H+JJ}}|m_{4\ell})} \right]^{-1} & \mathcal{D}_{\text{ZH}} &= \left[ 1 + \frac{\mathcal{P}_{\text{HJJ}}(\vec{\Omega}^{\text{H+JJ}}|m_{4\ell})}{\mathcal{P}_{\text{ZH}}(\vec{\Omega}^{\text{H+JJ}}|m_{4\ell})} \right]^{-1} \end{aligned} \quad (4)$$

where  $\mathcal{P}_{\text{VBF}}$ ,  $\mathcal{P}_{\text{HJJ}}$ ,  $\mathcal{P}_{\text{HJ}}$  and  $\mathcal{P}_{\text{VH}}$  are probabilities obtained from the JHUGEN matrix elements for the VBF process, the ggH (technically combination of gg/qg/qq' parton collisions) in association with two jets (H + 2jets), the ggH in association with one jet (H + 1jet), and the VH process. The  $\int d\eta_j \mathcal{P}_{\text{VBF}}$  is the integral of the two-jet VBF matrix element probability discussed above over the  $\eta_j$  values of the unobserved jet with the constraint that the total transverse momentum of the H + 2 jets system is zero. The  $\mathcal{D}_{\text{VH}}$ , used for event categorization, is simply defined as the maximum value of two discriminants  $\mathcal{D}_{\text{VH}} = \max(\mathcal{D}_{\text{ZH}}, \mathcal{D}_{\text{WH}})$ .

## 6 Event categorization

In order to improve the sensitivity to the H boson production mechanisms, the selected events are classified into mutually exclusive categories based on the features of the reconstructed objects associated with the  $\text{H} \rightarrow 4\ell$  candidates. This categorization is primarily designed to separate ggH, VBF, VH, and  $\text{t}\bar{\text{t}}\text{H}$ . There is little sensitivity to  $\text{b}\bar{\text{b}}\text{H}$  or  $\text{tH}$ , even though these production modes are also considered explicitly in this analysis. In addition, the events are further binned within the three main production mechanism (ggH, VBF, and VH) in order to study deeper structure within each production mechanisms, following the so-called Simplified Template Cross Sections (STXS) approach [25], which is also outlined in Figs. 1, 2, and 3. In the following, the Stage 1.1 of the STXS approach is adopted.

### 6.1 Truth-matched production Bin

STXS [25] were developed to provide finely-grained measurements compared to the signal strength and multiplicative coupling modifiers. The primary goals of the STXS framework are to maximize the sensitivity of the measurements while at the same time to minimize their dependence on the theory predictions. The measured exclusive regions of phase space, called Bins for simplicity, are specific to the different production modes. To account for the evolving experimental sensitivity, the STXS Bins are defined in stages (corresponding to increasingly fine granularity). The Stage 0 Bins correspond to the H boson production mechanisms. The previous Run 2 analysis has reported the measured Stage 0 results [15]. With the full Run 2 data, the current analysis targets the finer Stage 1.1 Bins. The Bin definitions are shown in Figs. 1, 2 and 3 and are discussed in more detail below.

The Bins in the STXS approach are identified at generator level using truth information in the MC simulation. We generally follow the approach described in Figs. 1, 2, and 3, with the  $\text{t}\bar{\text{t}}\text{H}$ ,  $\text{b}\bar{\text{b}}\text{H}$  and  $\text{tH}$  events left without further splitting [25]. Bins are identified using the truth H boson, truth vector bosons, and truth jets, defined as anti- $k_{\text{T}}$  jets with a distance parameter of 0.4 and a  $p_{\text{T}}$  threshold of 30 GeV.

The ggH process is split into events with  $p_{\text{T}}^{\text{H}} > 200$  GeV, with the Bin called  $\text{ggH}/p_{\text{T}} > 200$ . The events with zero or one jets are placed into Bins  $\text{ggH-0j}/p_{\text{T}}[0, 10]$ ,  $\text{ggH-0j}/p_{\text{T}}[10-200]$ ,  $\text{ggH-1j}/p_{\text{T}}[0-60]$ ,  $\text{ggH-1j}/p_{\text{T}}[60-120]$ , and  $\text{ggH-1j}/p_{\text{T}}[120-200]$ . The events with two or more jets are split according to the dijet invariant mass as follows. The events with



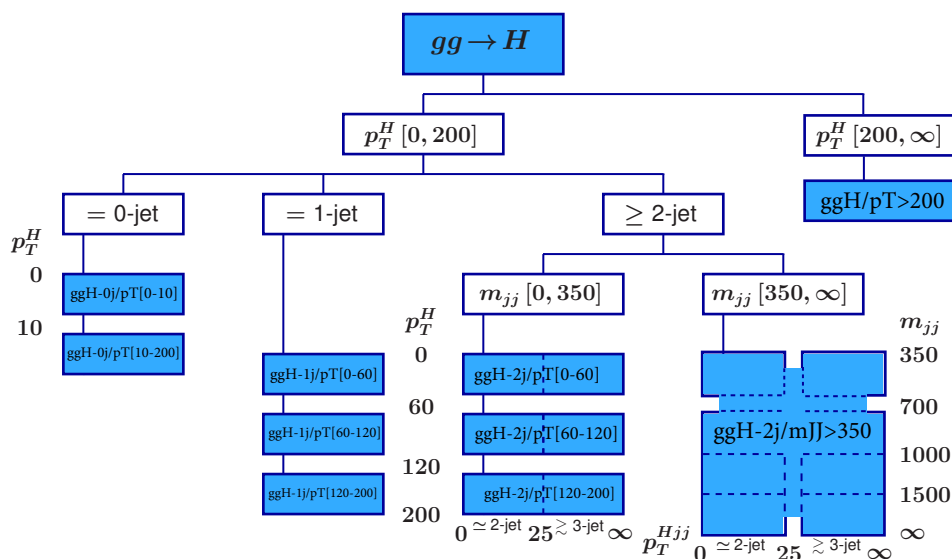


Figure 1: Binning of the gluon fusion production in the STXS Stage 1.1 approach [25].

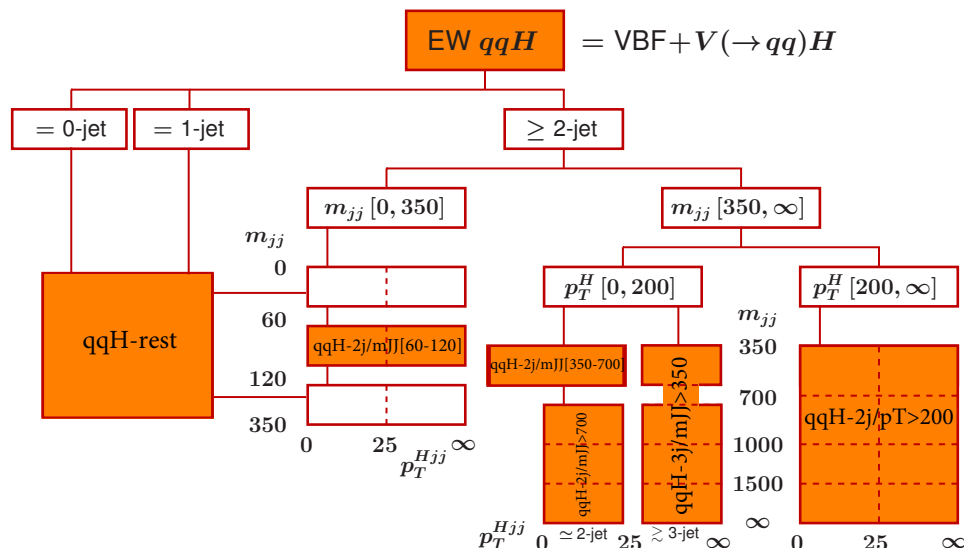


Figure 2: Binning of the electroweak production (combines VBF and VH with hadronic V decay) in the STXS Stage 1.1 approach [25].

$m_{JJ} < 350$  GeV are split into three Bins according to the H boson  $p_T$ :  $ggH-2j/p_T[0-60]$ ,  $ggH-2j/p_T[60-120]$ , and  $ggH-2j/p_T[120-200]$ . The events with  $m_{JJ} > 350$  GeV are all placed into one Bin  $ggH-2j/m_{JJ}>350$ , which merges four Bins originally suggested in Fig. 1. The latter merging is needed because of the very low event count expected in this Bin.

The electroweak process Bins are sketched in Fig. 2 and are labeled with  $q\bar{q}H$  to represent production of the H boson in association with two quarks from either VBF or VH processes

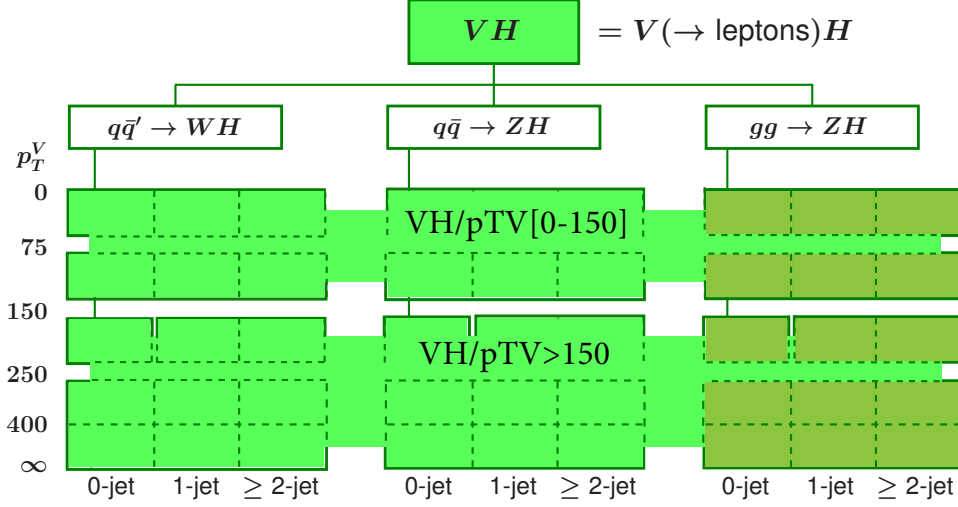


Figure 3: Binning of the VH production with leptonic V decay (combining WH, ZH, and gluon fusion ZH production) in the STXS Stage 1.1 approach [25].

with hadronic decay of the V. While these VBF and VH processes are merged into common Bins for the purpose of the STXS approach, they are separated for the dedicated fits for the VBF and VH strengths. There are six shaded boxes and four open boxes identified in Fig. 2. All open boxes (for 0-jet, 1-jet, or with two or more jets with  $m_{JJ} < 60$  GeV or  $120 < m_{JJ} < 350$  GeV) represent the Bins of secondary importance in the STXS approach and they are all merged into one Bin qqH-rest in this analysis. The events with  $60 < m_{JJ} < 120$  GeV are called qqH-2j/mJJ[60-120]. The events with two or more jets and  $p_T^H > 200$  GeV are called qqH-2j/pT>200. The events with  $p_T^{HJJ} > 25$  GeV are labeled as 3-jet and called qqH-3j/mJJ>350. This Bin merges two  $m_{JJ}$  Bins identified in Fig. 2, because of the low expected yield. The remaining two Bins qqH-2j/mJJ[350, 700] and qqH-2j/mJJ>700 correspond to  $p_T^{HJJ} < 25$  GeV.

The VH process Bins with leptonic V decay are shown in Fig. 3. First of all, the three processes are combined together: WH, ZH, and gluon fusion ZH production. Second, several proposed Bins are merged together into two Bins according to  $p_T$  of the vector boson: VH/pTV[0-150] and VH/pTV>150.

The last three processes remain without further splitting: ttH, bbH, tH. However, due to low expected yield and lack of distinguishing features, the bbH Bin is merged into the ggH-0j/pT[10-200] Bin, which resembles kinematics of these events the most. For the same reasons, the tH Bin is merged into ttH.

## 6.2 Reconstructed Event Categories

Category definitions exploit the multiplicity of jets, b-tagged jets and additional leptons (defined as leptons that are not involved in the ZZ candidate selection and that pass identification, vertex compatibility, and isolation requirements), requirements on the kinematic discriminants described in Section 5, invariant mass of the two leading jets, and the transverse momentum of the ZZ candidate.

Categorization is done in two steps. In the first step, seven categories are defined in the same way as previous Run 2 analyses [15], except that in the VBF-1jet-tagged category,  $\mathcal{D}_{1\text{jet}}$  require-

ment is shifted from 0.5 to 0.7 to improve the purity. This categorization has been optimized for precision to determine the main production modes of the H boson. In the second step, finer sub-categories are defined within each category, to identify the STXS Stage 1.1 Bins from reconstructed data.

In the first step, the criteria are applied in this exact order as follows (i.e. an event is considered for the subsequent category only if it does not satisfy the requirements of the previous category):

- **VBF-2jet-tagged category** requires exactly 4 leptons. In addition there must be either 2 or 3 jets of which at most 1 is b-tagged, or at least 4 jets and no b-tagged jets. Finally,  $\mathcal{D}_{2\text{jet}} > 0.5$  is required.
- **VH-hadronic-tagged category** requires exactly 4 leptons. In addition there must be 2 or 3 jets, or at least 4 jets and no b-tagged jets. Finally,  $\mathcal{D}_{\text{VH}} > 0.5$  is required.
- **VH-leptonic-tagged category** requires no more than 3 jets and no b-tagged jets in the event, and exactly 1 additional lepton or 1 additional pair of opposite sign same flavor leptons. This category also includes events with no jets and at least 1 additional lepton.
- **t $\bar{t}$ H-hadronic-tagged category** requires at least 4 jets of which at least 1 is b-tagged and no additional leptons.
- **t $\bar{t}$ H-leptonic-tagged category** requires at least 1 additional lepton in the event.
- **VBF-1jet-tagged category** requires exactly 4 leptons, exactly 1 jet and  $\mathcal{D}_{1\text{jet}} > 0.7$ .
- **Untagged category** consists of the remaining events.

Figure 4 shows the signal relative purity of the seven event categories in terms of H boson production processes following seven categories defined in the first step.

In the second step, the following 22 sub-categories are introduced, which are designed to match the STXS Bins defined above, and therefore their names overlap. However, since truth matching of the Bins and reconstruction of the category information cannot match exactly, there is no one-to-one correspondence between Bins and sub-categories. These sub-categories are defined as follows:

- **Untagged category:**
  1. ggH/pT>200: the Higgs boson has  $p_T^H > 200$  GeV;
  2. ggH-0j/pT[0,10]: 0 jet reconstructed and  $0 < p_T^H < 10$  GeV;
  3. ggH-0j/pT[10-200]: 0 jet reconstructed and  $10 < p_T^H < 200$  GeV;
  4. ggH-1j/pT[0-60]: 1 jet reconstructed and  $0 < p_T^H < 60$  GeV;
  5. ggH-1j/pT[60-120]: 1 jet reconstructed and  $60 < p_T^H < 120$  GeV;
  6. ggH-1j/pT[120-200]: 1 jet reconstructed and  $120 < p_T^H < 200$  GeV;
  7. ggH-2j/mJJ>350: 2 jets reconstructed and  $m_{jj} > 350$  GeV;
  8. ggH-2j/pT[0-60]: 2 jets reconstructed,  $0 < p_T^H < 60$  GeV, and  $m_{jj} < 350$  GeV;
  9. ggH-2j/pT[60-120]: 2 jets reconstructed,  $60 < p_T^H < 120$  GeV, and  $m_{jj} < 350$  GeV;
  10. ggH-2j/pT[120-200]: 2 jets reconstructed,  $120 < p_T^H < 200$  GeV, and  $m_{jj} < 350$  GeV.

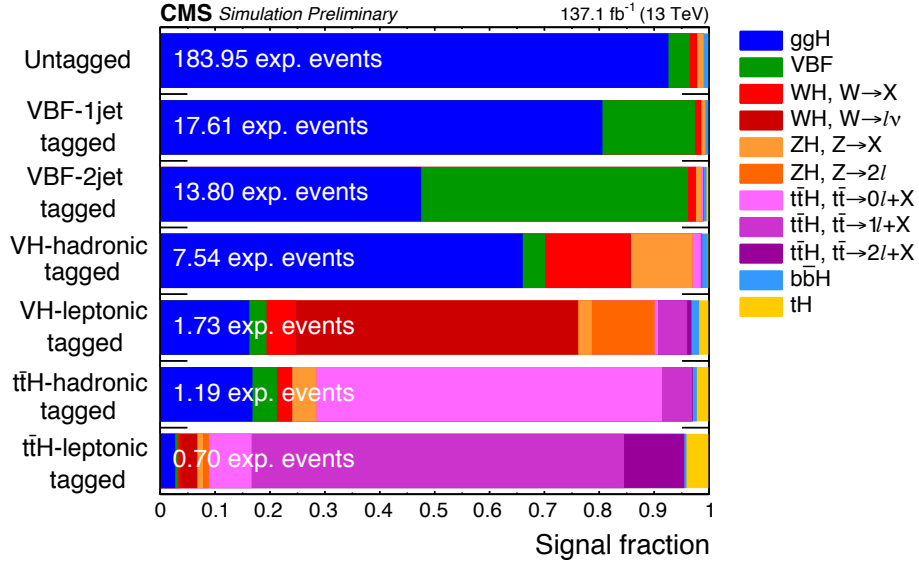


Figure 4: Signal relative purity of the event categories in terms of the seven main production mechanisms of the Higgs boson in a  $118 < m_{4\ell} < 130$  GeV mass window. The WH, ZH and ttH processes are split according to the decay of associated objects, whereby X denotes anything other than an electron or muon.

- **VBF-1jet-tagged category:** VBF-1 j
- **VBF-2jet-tagged category:**
  1. VBF-2 j/ $p_T^H > 200$ :  $p_T^H > 200$  GeV and  $m_{jj} > 350$  GeV;
  2. VBF-2 j/ $m_{JJ}[350, 700]$ :  $p_T^H < 200$  GeV,  $p_T^{Hjj} < 25$  GeV, and  $350 < m_{jj} < 700$  GeV;
  3. VBF-2 j/ $m_{JJ} > 700$ :  $p_T^H < 200$  GeV,  $p_T^{Hjj} < 25$  GeV,  $m_{jj} > 700$  GeV;
  4. VBF-3 j/ $m_{JJ} > 350$ :  $p_T^H < 200$  GeV,  $p_T^{Hjj} > 25$  GeV,  $m_{jj} > 350$  GeV;
  5. VBF-rest: if not above.
- **VH-hadronic-tagged category**
  1. VH-had/ $m_{JJ}[60-120]$ :  $60 < m_{jj} < 120$  GeV;
  2. VH-rest: not above.
- **VH-leptonic-tagged category**
  1. VH-lep/ $p_T[0-150]$ :  $p_T^H < 150$  GeV;
  2. VH-lep/ $p_T > 150$ :  $p_T^H > 150$  GeV.
- **ttH-hadronic-tagged category:** ttH-had.
- **ttH-leptonic-tagged category:** ttH-lep.

Figure 5 shows the signal relative purity of all STXS Stage 1.1 Bins in the 22 event sub-categories defined above.

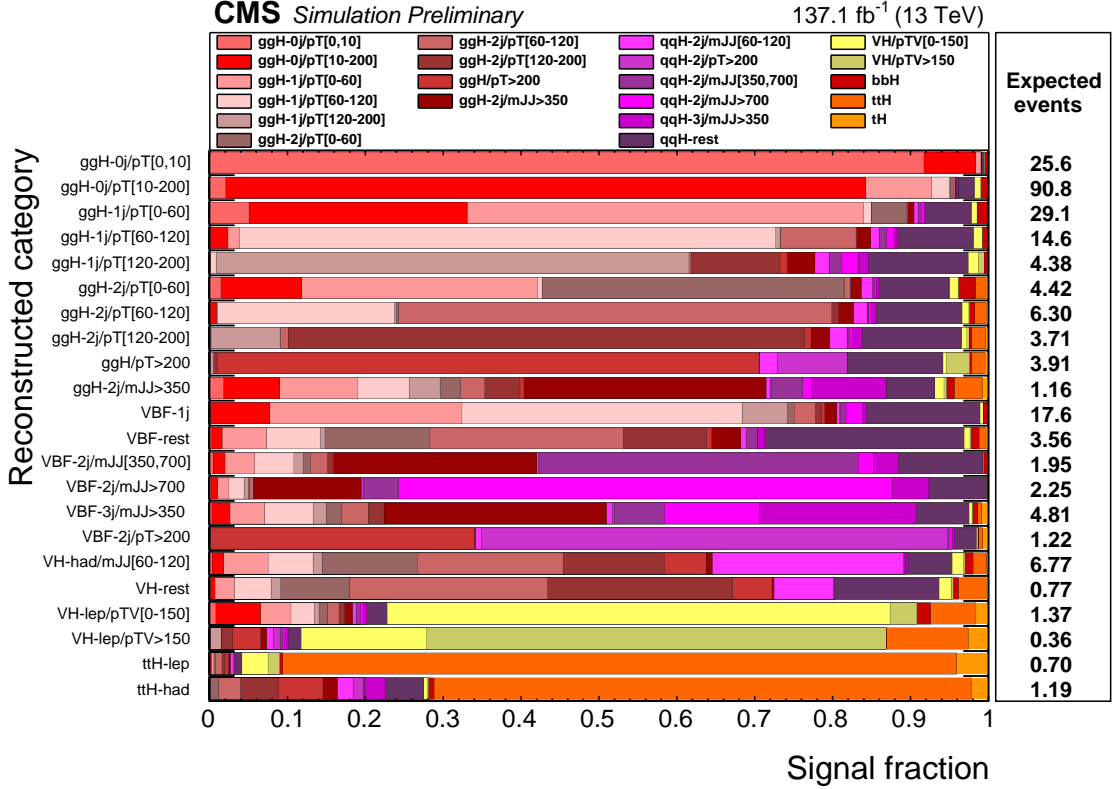


Figure 5: Signal relative purity of the 22 event sub-categories in terms of the STXS Stage 1.1 Bins in a  $118 < m_{4\ell} < 130$  GeV mass window.

## 7 Background estimation

### 7.1 Irreducible backgrounds

The irreducible background to the H boson signal in the  $4\ell$  channel, which come from the production of  $ZZ$  via  $q\bar{q}$  annihilation or gluon fusion, is estimated using simulation. The fully differential cross section for the  $q\bar{q} \rightarrow ZZ$  process has been computed at NNLO [55], and the NNLO/NLO K factor as a function of  $m_{ZZ}$  has been applied to the POWHEG sample. This K factor varies from 1.0 to 1.2 and is 1.1 at  $m_{ZZ} = 125$  GeV. Additional NLO electroweak corrections which depend on the initial state quark flavor and kinematics are also applied in the region  $m_{ZZ} > 2m_Z$  following the prescription in [56].

The production of  $ZZ$  via gluon fusion contributes at NNLO in pQCD. It has been shown [57] that the soft collinear approximation is able to describe the background cross section and the interference term at NNLO. Further calculations also show that the K factors are very similar at NLO for the signal and background [58] and at NNLO for the signal and interference terms [59]. Therefore, the same K factor is used for the signal and background [60]. The NNLO K factor for the signal is obtained as a function of  $m_{ZZ}$  using the HNNLO v2 program [61–63] by calculating the NNLO and LO  $gg \rightarrow H \rightarrow 2\ell 2\ell'$  cross sections at the small H boson decay width of 4.07 MeV and taking their ratios. The NNLO/LO K factor for  $gg \rightarrow ZZ$  varies from 2.0 to 2.6 and is 2.27 at  $m_{ZZ} = 125$  GeV, and a systematic uncertainty of 10% on its determination is used in the analysis when applied to the background process.

## 7.2 Reducible backgrounds

Additional backgrounds to the H boson signal in the  $4\ell$  channel arise from processes in which heavy-flavor jets produce secondary leptons, and also from processes in which decays of heavy-flavor hadrons, in-flight decays of light mesons within jets, or (for electrons) the decay of charged hadrons overlapping with  $\pi^0$  decays are misidentified as leptons. The main processes producing these backgrounds are  $Z + \text{jets}$ ,  $t\bar{t} + \text{jets}$ ,  $Z\gamma + \text{jets}$ ,  $WW + \text{jets}$ , and  $WZ + \text{jets}$ . We denote these reducible backgrounds as “Z+X” since they are dominated by the  $Z + \text{jets}$  process. The contribution from the reducible background is estimated using two independent methods having dedicated control regions in data. The control regions are defined by a dilepton pair satisfying all the requirements of a  $Z_1$  candidate and two additional leptons, opposite sign (OS) or same sign (SS), satisfying certain relaxed identification requirements when compared to those used in the analysis. These four leptons are then required to pass the analysis ZZ candidate selection. The event yield in the signal region is obtained by weighting the control region events by the lepton misidentification probability  $f_e$  (resp.  $f_\mu$ ), defined as the fraction of non-signal electrons (resp. muons) which are identified by the analysis selection criteria. A detailed description of both methods can be found in Ref. [14].

The lepton misidentification rates  $f_e$  and  $f_\mu$  are measured by forming a sample which includes a  $Z_1$  candidate consisting of a pair of leptons, both passing the selection requirements used in the analysis, and exactly one additional lepton passing the relaxed selection.

For the OS method, the mass of the  $Z_1$  candidate is required to satisfy  $|Z_1 - m_Z| < 7$  GeV in order to reduce the contribution of (asymmetric) photon conversions which is estimated separately. In the SS method, the contribution of photon conversions to the misidentification rate is estimated with dedicated samples and corrected for. Furthermore, the  $p_T^{\text{miss}}$  is required to be less than 25 GeV in order to suppress contamination from WZ and  $t\bar{t}$  processes.

### 7.2.1 Prediction and uncertainties

The predicted yield in the signal region of the reducible background from the two methods are in agreement within their uncertainties, and since they are mutually independent, the results of the two methods are combined. The shape of the  $m_{4\ell}$  distribution for the reducible background is obtained by combining the prediction from the OS and SS methods and fitting the distributions with empirical functional forms built from Landau [64] and exponential distributions.

The dominant systematic uncertainty on the reducible background estimation arises from the limited number of events in the control regions as well as in the region where the misidentification rates are computed. Additional sources of systematic uncertainty arise from the difference in the composition of the sample from which the misidentification rate is computed and the control regions of the two methods where the misidentification rate is applied.

## 8 Signal modeling

In order to generate an accurate signal model, the  $p_T$  spectrum of the H boson ( $p_T(\text{H})$ ) was tuned in the POWHEG simulation of the dominant gluon fusion production mode to better match predictions from full phase space calculations implemented in the HRES 2.3 generator [63, 65, 66].

In order to take advantage of the most accurate simulation of ggH available, a reweighting is defined. Events from ggH are separated into 0, 1, 2, and  $\geq 3$  jet bins, where the jets used for counting are clustered from all stable particles, excluding the decay products of the H boson or

associated vector bosons, and have  $p_T > 30$  GeV. The sum of weights in each sample are first normalized to the inclusive cross section. The ratio of the  $p_T(H)$  distribution from the NNLOPS generator [67] to that from the POWHEG generator in each jet bin is applied to the ggH signal samples.

The signal lineshape of a narrow resonance around  $m_H \sim 125$  GeV is parametrized using a double-sided Crystal Ball function [16]. In addition, a Landau function is also added in the total probability density function for the non-resonant part of the signal for the case of WH, ZH and  $t\bar{t}H$  production modes. The signal lineshape is parametrized as a function of  $m_H$  by performing a simultaneous fit of several mass points for ggH production in mass range from 105 GeV to 140 GeV. Each parameter of the double-sided Crystal Ball function is given a linear dependence on  $m_H$  for a total of 12 free parameters. The correlation amongst these 12 parameters is checked and parameters are dropped to remove large correlations, or if they are constant within the uncertainty.

## 9 Systematic uncertainties

The experimental uncertainties common to all final states include the uncertainty in the integrated luminosity (from 2.3% to 2.5%, depending on the year of data taking) and the uncertainty in the lepton identification and reconstruction efficiency (ranging from 2.5 to 16.1% on the overall event yield for the  $4\mu$  and  $4e$  channels, respectively), which affect both signal and background. Experimental uncertainties in the reducible background estimation, described in Section 7.2, originating from the background composition and misidentification rate uncertainty vary between 24 and 43% depending on the final state and category. The uncertainty in the lepton energy scale is determined by considering the  $Z \rightarrow \ell\ell$  mass distributions in data and simulation. Events are separated into categories based on the  $p_T$  and  $\eta$  of one of the two leptons, determined randomly, and integrating over the other. The dilepton mass distributions are then fit by a Breit-Wigner parameterization convolved with a double-sided Crystal Ball function.

Theoretical uncertainties which affect both the signal and background estimation include uncertainties from the renormalization and factorization scale and choice of PDF set. The uncertainty from the renormalization and factorization scale is determined by varying these scales between 0.5 and 2 times their nominal value while keeping their fraction between 0.5 and 2. The uncertainty from the PDF set is determined by taking the root mean square of the variation when using different replicas of the default NNPDF set. An additional uncertainty of the 10% in the K factor used for the  $gg \rightarrow ZZ$  prediction is applied as described in Section 7.1. A systematic uncertainty of 2% [24] in the branching fraction of  $H \rightarrow 4\ell$  only affects the signal yield. The theoretical uncertainties on the background yield are included for all measurements, while the theoretical uncertainties on the overall signal yield are not included in the measurement uncertainties when cross sections, rather than signal strengths, are extracted.

The ggH cross section uncertainty scheme has been updated to the one proposed in Ref. [24]. This uncertainty scheme includes 9 nuisance parameters accounting for uncertainties in the cross section prediction for exclusive jet bins (including the migration between the 0 and 1-jet, as well as between the 1 and  $\geq 2$ -jet bins), the 2 jet and  $\geq 3$  jet VBF phase spaces, different  $p_T(H)$  regions, and the uncertainty in the  $p_T(H)$  distribution due to missing higher order finite top quark mass corrections.

All experimental and theoretical uncertainties which account for possible migration of signal and background events between categories are included. The main theoretical sources of un-

certainty on the event categorization include the renormalization and the factorization scales, the choice of the PDF set, and the modeling of hadronization and the underlying event. For example, uncertainty on the renormalization and factorization scale for dominant ggH production mode ranges from 0.1 to 6% and for VBF production mode from 0.1 to 12% depending on the event category. The modeling of hadronization and the underlying event ranges from 1 to 50% in event categories with 2 jets, from 1 to 20% in event categories with 1 jet, and from 1 to 15% in event categories with no jets.

The main experimental sources of category migration come from the imprecise knowledge of the jet energy scale and resolution, b-tagging efficiency, and light quarks (u, d, s, c) and gluon jet mistag rate. For example, uncertainty on the jet energy scale ranges from 2 to 50% for VBF production mode in event categories with jets and the uncertainty on b-tagging efficiency ranges from 1 to 2% for ttH production and 1 to 10% for ggH production in the ttH-hadronic-tagged category.

In the combination of the three data taking periods, the theoretical uncertainties as well as the experimental ones related to leptons or jets are treated as correlated while all other ones from experimental sources are taken as uncorrelated.

## 10 Results

The reconstructed four-lepton invariant mass distribution is shown for data collected in 2018 in Fig. 6 and for full Run 2 in Fig. 7 for the sum of the 4e, 4 $\mu$  and 2e2 $\mu$  subchannels, and compared with the expectations from signal and background processes. The error bars on the data points correspond to the so-called Garwood confidence intervals at 68% confidence level (CL) [68]. The observed distribution agrees with the expectation within the statistical uncertainties over the whole spectrum. The Fig. 8 shows number of expected and observed events in all Stage 1.1 sub-categories for full Run 2.

The number of candidates observed in data and the expected yields for 59.7 fb<sup>-1</sup> of data collected in 2018, for the backgrounds and Higgs boson signal after the full event selection are reported in Table 1 for the full range of  $m_{4\ell}$ . Table 2 shows the expected and observed yields for each of the 22 event sub-categories for a 118 <  $m_{4\ell}$  < 130 GeV mass window around the Higgs boson peak for full Run 2.

Table 1: The number of expected background and signal events and number of observed candidates after full analysis selection, for each final state, for the full mass range  $m_{4\ell} > 70$  GeV and for an integrated luminosity of 59.7 fb<sup>-1</sup>. Signal and ZZ backgrounds are estimated from Monte Carlo simulation, Z+X is estimated from data. The uncertainties include both statistical and systematic sources.

Channel	4e	4 $\mu$	2e2 $\mu$	4 $\ell$
q $\bar{q}$ $\rightarrow$ ZZ	333 <sup>+57</sup> <sub>-53</sub>	622 <sup>+31</sup> <sub>-44</sub>	815 $\pm$ 73	1770 <sup>+98</sup> <sub>-101</sub>
gg $\rightarrow$ ZZ	75.1 <sup>+14.3</sup> <sub>-13.5</sub>	116.6 <sup>+11.7</sup> <sub>-12.8</sub>	176.9 $\pm$ 23.0	368.5 <sup>+29.5</sup> <sub>-29.6</sub>
Z + X	19.3 $\pm$ 7.2	50.8 $\pm$ 15.2	64.6 $\pm$ 15.6	134.7 $\pm$ 22.9
Sum of backgrounds	428 <sup>+59.2</sup> <sub>-55.2</sub>	790 <sup>+36.4</sup> <sub>-48.3</sub>	1057 $\pm$ 78.1	2274 <sup>+104.9</sup> <sub>-107.7</sub>
Signal ( $m_H = 125$ GeV)	19.6 <sup>+3.3</sup> <sub>-3.1</sub>	40.8 <sup>+2.5</sup> <sub>-2.9</sub>	50.7 $\pm$ 5.6	111.1 <sup>+6.9</sup> <sub>-7.0</sub>
Total expected	447 <sup>+59.3</sup> <sub>-55.2</sub>	830 <sup>+36.5</sup> <sub>-48.4</sub>	1108 $\pm$ 78.3	2385 <sup>+105.1</sup> <sub>-107.9</sub>
Observed	462	850	1130	2442

The reconstructed dilepton invariant masses selected as  $Z_1$  and  $Z_2$  are shown in Fig. 9 for 118 <



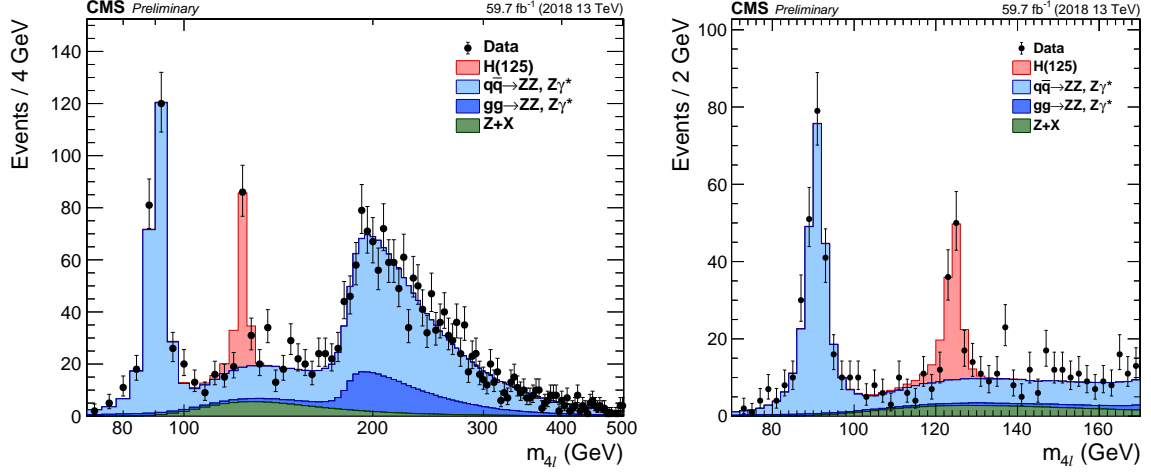


Figure 6: Distribution of the reconstructed four-lepton invariant mass  $m_{4\ell}$  up to 500 GeV (left) and the low-mass range (right), with 2018 data. Points with error bars represent the data and stacked histograms represent expected distributions of the signal and background processes. The SM Higgs boson signal with  $m_H = 125$  GeV, denoted as H(125), and the ZZ backgrounds are normalized to the SM expectation, the Z+X background to the estimation from data. The order in perturbation theory used for the normalization of the irreducible backgrounds is described in Section 7.1.

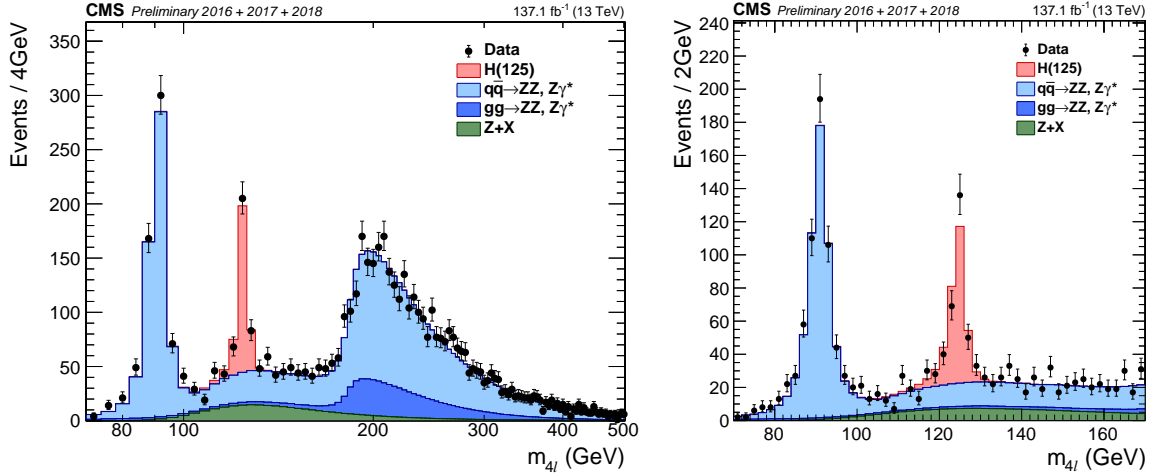


Figure 7: Distribution of the reconstructed four-lepton invariant mass  $m_{4\ell}$  up to 500 GeV (left) and the low-mass range (right), with full Run 2 data. Points with error bars represent the data and stacked histograms represent expected distributions of the signal and background processes. The SM Higgs boson signal with  $m_H = 125$  GeV, denoted as H(125), and the ZZ backgrounds are normalized to the SM expectation, the Z+X background to the estimation from data. The order in perturbation theory used for the normalization of the irreducible backgrounds is described in Section 7.1.

$m_{4\ell} < 130$  GeV, with their correlation. The distribution of the discriminants used for event categorization along with the corresponding working point values are shown in Fig. 10. The correlation of the kinematic discriminants  $\mathcal{D}_{\text{bkg}}^{\text{kin}}$ ,  $\mathcal{D}_{\text{bkg}}^{\text{VBF+dec}}$  and  $\mathcal{D}_{\text{bkg}}^{\text{VH+dec}}$  with the four-lepton

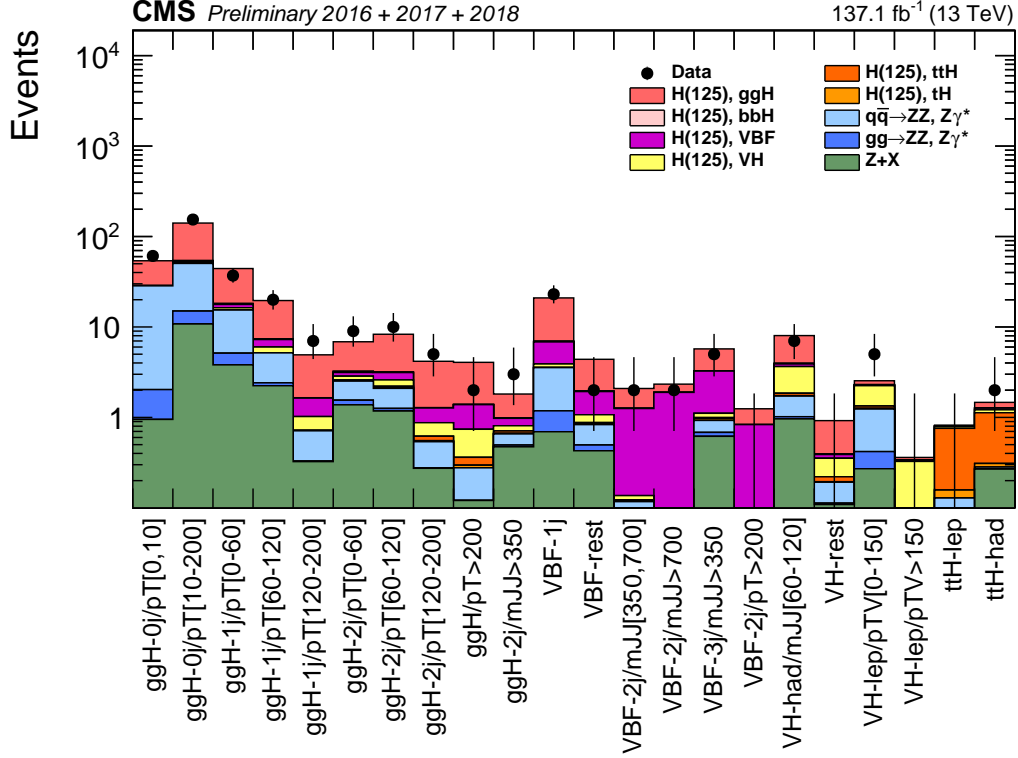


Figure 8: Distributions of the expected and observed number of events for all Stage 1.1 sub-categories described in Section 6.2 in the mass region  $118 < m_{4\ell} < 130$  GeV with Run 2 data. Points with error bars represent the data and stacked histograms represent the expected numbers of the signal and background events. The different SM Higgs boson signal production modes with  $m_H = 125$  GeV, denoted as H(125), and the ZZ backgrounds are normalized to the SM expectation, the Z+X background to the estimation from data. The order in perturbation theory used for the normalization of the irreducible backgrounds is described in Section 7.1.

invariant mass is shown in Fig. 11. Their distributions for  $118 < m_{4\ell} < 130$  GeV are shown in Fig. 12.

### 10.1 Signal strength

To extract the signal strength for the excess of events observed in the H boson peak region, we perform a multi-dimensional fit that relies on two variables: the four-lepton invariant mass  $m_{4\ell}$  and the  $\mathcal{D}_{\text{bkg}}^{\text{kin}}$  discriminant. We define the two-dimensional likelihood function as:

$$\mathcal{L}_{2D}(m_{4\ell}, \mathcal{D}_{\text{bkg}}^{\text{kin}}) = \mathcal{L}(m_{4\ell})\mathcal{L}(\mathcal{D}_{\text{bkg}}^{\text{kin}}|m_{4\ell}). \quad (5)$$

The kinematic discriminant is different for each category. In sub-categories of the VBF-2jet-tagged category defined in Section 6.2, we use  $\mathcal{D}_{\text{bkg}}^{\text{VBF+dec}}$  which is sensitive to the VBF production mechanism. Similarly, in two sub-categories of the VH-hadronic-tagged category the  $\mathcal{D}_{\text{bkg}}^{\text{VH+dec}}$  discriminant is used. In all other sub-categories we use a decay only kinematic discriminant to separate H boson signal from the background. The mass dimension is unbinned and uses the model described in Section 8. The conditional 2D term is implemented by creating a two-dimensional template of  $m_{4\ell}$  vs.  $\mathcal{D}_{\text{bkg}}^{\text{kin}}$  normalized to 1 for each bin of  $m_{4\ell}$ . ggH, VBF, WH

Table 2: The number of expected background and signal events and number of observed candidates after full analysis selection, for each event category, for the mass range  $118 < m_{4\ell} < 130$  GeV and for an integrated luminosity of  $137.1 \text{ fb}^{-1}$ . The yields are given for the different production modes. Signal and ZZ backgrounds are estimated from Monte Carlo simulation, Z+X is estimated from data. The uncertainties include both statistical and systematic sources.

Event category	Signal							Total signal	Background			Total expected	Observed
	ggH	VBF	WH	ZH	ttH	bbH	tqH		$q\bar{q} \rightarrow ZZ$	$gg \rightarrow ZZ$	Z + X		
ggH-0j/pT[0,10]	25.3	0.08	0.02	0.02	0.00	0.14	0.00	25.6	26.5	0.97	1.19	54.2	61
ggH-0j/pT[10-200]	86.8	1.69	0.54	0.86	0.00	0.90	0.00	90.8	35.4	3.79	15.5	145	153
ggH-1j/pT[0-60]	26.2	1.43	0.50	0.45	0.01	0.43	0.01	29.1	10.3	1.19	5.54	46.1	40
ggH-1j/pT[60-120]	12.4	1.24	0.45	0.47	0.01	0.10	0.01	14.6	2.76	0.16	3.21	20.8	17
ggH-1j/pT[120-200]	3.31	0.62	0.17	0.26	0.00	0.02	0.00	4.38	0.38	0.00	0.52	5.28	6
ggH-2j/pT[0-60]	3.68	0.29	0.14	0.14	0.06	0.09	0.02	4.42	0.97	0.15	2.07	7.60	9
ggH-2j/pT[60-120]	5.17	0.54	0.22	0.22	0.09	0.04	0.02	6.30	0.84	0.07	1.86	9.06	12
ggH-2j/pT[120-200]	2.90	0.40	0.15	0.17	0.07	0.01	0.02	3.71	0.26	0.00	0.40	4.37	5
ggH/pT>200	2.72	0.65	0.21	0.24	0.06	0.01	0.02	3.91	0.16	0.00	0.21	4.28	2
ggH-2j/mJJ>350	0.82	0.17	0.06	0.05	0.04	0.01	0.01	1.16	0.16	0.02	0.65	1.98	3
VBF-1j	14.2	2.94	0.20	0.18	0.00	0.12	0.01	17.6	2.37	0.43	1.05	21.5	20
VBF-2j/mJJ[350,700]	0.80	1.11	0.01	0.01	0.00	0.01	0.00	1.95	0.08	0.02	0.04	2.09	2
VBF-2j/mJJ>700	0.43	1.80	0.00	0.00	0.00	0.00	0.00	2.25	0.02	0.01	0.03	2.31	2
VBF-3j/mJJ>350	2.43	2.15	0.06	0.07	0.02	0.03	0.05	4.81	0.24	0.06	0.96	6.07	6
VBF-2j/pT>200	0.42	0.76	0.01	0.01	0.01	0.00	0.01	1.22	0.01	0.00	0.03	1.26	0
VBF-rest	2.40	0.87	0.11	0.10	0.03	0.04	0.01	3.56	0.34	0.06	0.74	4.70	2
VH-lep/pTV[0-150]	0.24	0.04	0.71	0.25	0.08	0.02	0.02	1.37	0.82	0.14	0.40	2.72	5
VH-lep/pTV>150	0.02	0.01	0.21	0.08	0.04	0.00	0.01	0.36	0.01	0.00	0.02	0.40	0
VH-had/mJJ[60-120]	4.11	0.25	1.01	1.20	0.11	0.07	0.02	6.77	0.70	0.05	1.36	8.89	8
VH-rest	0.56	0.04	0.08	0.07	0.03	0.00	0.00	0.77	0.08	0.00	0.15	1.01	1
ttH-had	0.19	0.05	0.03	0.06	0.82	0.01	0.03	1.19	0.01	0.00	0.45	1.66	2
ttH-lep	0.02	0.00	0.02	0.02	0.60	0.00	0.03	0.70	0.03	0.00	0.12	0.85	0

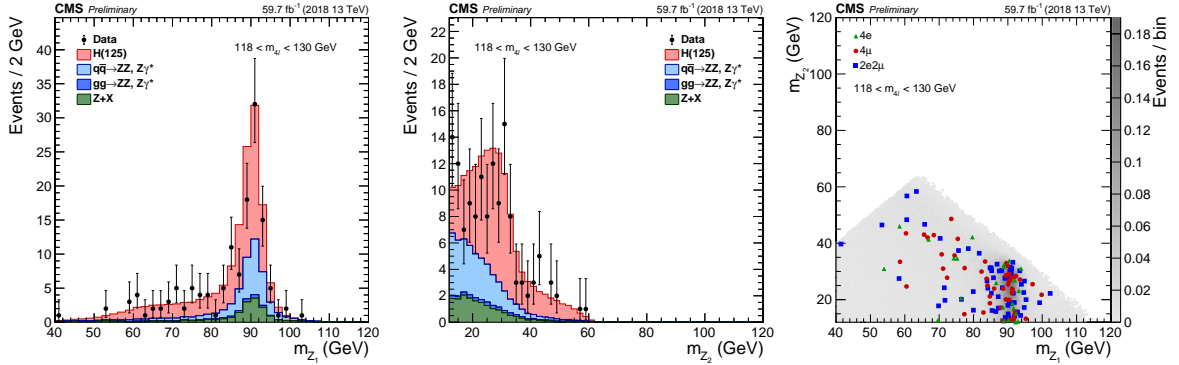


Figure 9: Distribution of the  $Z_1$  (left) and  $Z_2$  (center) reconstructed masses and correlation between the two (right) in the mass region  $118 < m_{4\ell} < 130$  GeV, with 2018 data. The stacked histograms and the gray scale represent expected distributions of the signal and background processes, and points represent the data. The SM Higgs boson signal with  $m_H = 125$  GeV, denoted as H(125), and the ZZ backgrounds are normalized to the SM expectation, the Z+X background to the estimation from data. The order in perturbation theory used for the normalization of the irreducible backgrounds is described in Section 7.1.

and ZH samples are used to build different templates for each of the corresponding production modes. For all other production modes ggH templates are used. The  $(m_{4\ell}, D_{\text{bkg}}^{\text{kin}})$  unbinned distributions of selected events are split into categories based on the twenty-two event categories and the three final states ( $4\mu$ ,  $4e$ ,  $2e2\mu$ ).

A simultaneous fit to all categories is performed to extract the signal-strength modifier, defined

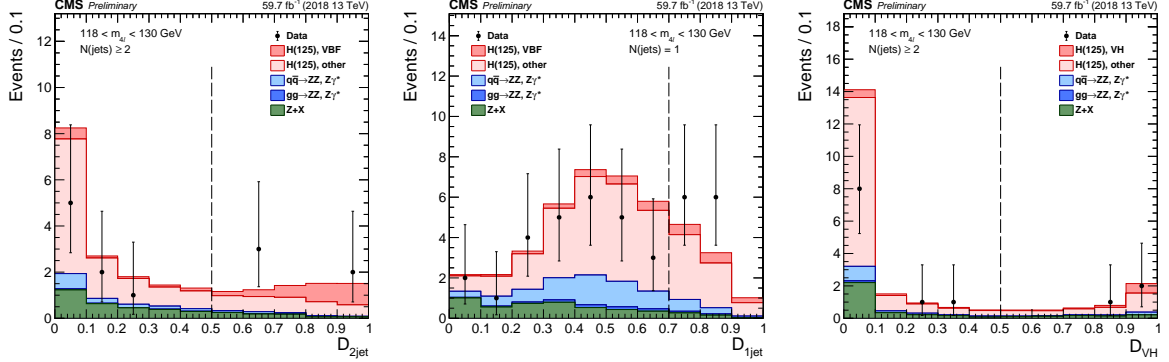


Figure 10: Distribution of categorization discriminants in the mass region  $118 < m_{4\ell} < 130$  GeV, with 2018 data: (left)  $D_{2\text{jet}}$ , (middle)  $D_{1\text{jet}}$ , (right)  $D_{\text{VH}} = \max(D_{\text{WH}}, D_{\text{ZH}})$ . Points with error bars represent the data and stacked histograms represent expected distributions of the signal and background processes. The SM Higgs boson signal with  $m_{\text{H}} = 125$  GeV, denoted as H(125), and the ZZ backgrounds are normalized to the SM expectation, the Z+X background to the estimation from data. The vertical gray dashed lines denote the working points used in the event categorization. The SM Higgs boson signal is separated into two components: the production mode which is targeted by the specific discriminant, and other production modes, where the gluon fusion process dominates. The order in perturbation theory used for the normalization of the irreducible backgrounds is described in Section 7.1.

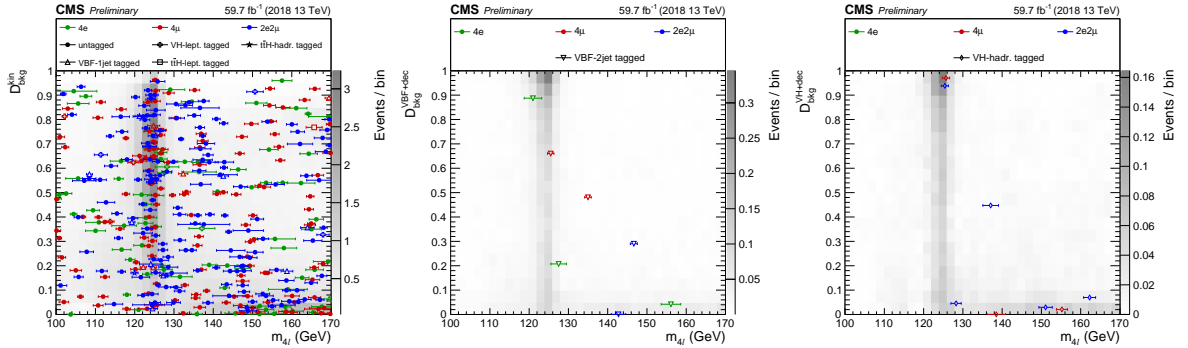


Figure 11: Distribution of three different kinematic discriminants versus  $m_{4\ell}$ , with 2018 data:  $D_{\text{bkg}}^{\text{kin}}$  (left),  $D_{\text{bkg}}^{\text{VBF+dec}}$  (middle) and  $D_{\text{bkg}}^{\text{VH+dec}}$  (right) shown in the mass region  $100 < m_{4\ell} < 170$  GeV. The gray scale represents the expected total number of ZZ and Z+X background and SM Higgs boson signal events for  $m_{\text{H}} = 125$  GeV. The points show the data and the horizontal bars represent the measured event-by-event mass uncertainties. Different marker styles are used to denote the categorization of the events.

as the ratio of the observed H boson rate in the  $\text{H} \rightarrow \text{ZZ} \rightarrow 4\ell$  decay channel to the standard model expectation. The combined result is  $\mu = \sigma/\sigma_{\text{SM}} = 0.94^{+0.11}_{-0.10}$  with  $m_{\text{H}}$  profiled in the fit. The dominant experimental sources of systematic uncertainty are the uncertainties in the lepton identification efficiencies and luminosity measurement, while the dominant theoretical source is the uncertainty in the total gluon fusion cross section. The contributions to the total uncertainty from experimental and theoretical sources are found to be similar in magnitude.

A fit is performed for four main signal-strength modifiers ( $\mu_{\text{ggH}, b\bar{b}\text{H}}$ ,  $\mu_{\text{VBF}}$ ,  $\mu_{\text{VH}}$ , and  $\mu_{\text{ttH}, \text{tH}}$ )

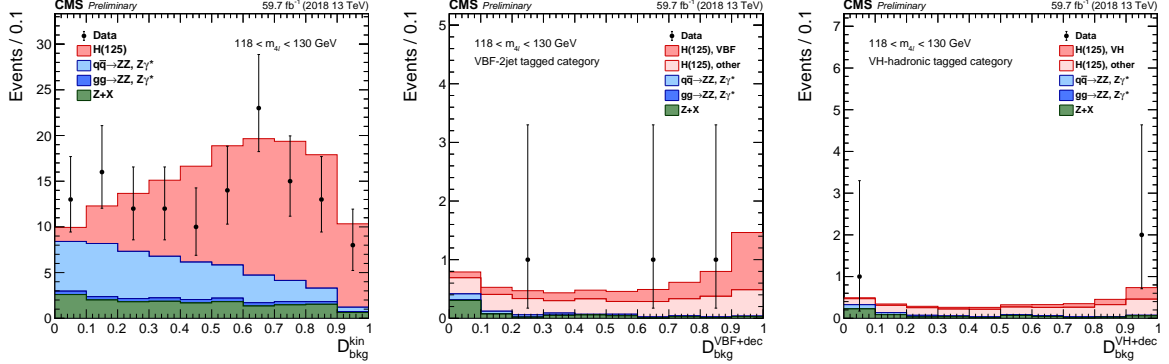


Figure 12: Distribution of kinematic discriminants in the mass region  $118 < m_{4\ell} < 130$  GeV, with 2018 data: (left)  $\mathcal{D}_{\text{bkg}}^{\text{kin}}$ , (middle)  $\mathcal{D}_{\text{bkg}}^{\text{VBF+dec}}$ , (right)  $\mathcal{D}_{\text{bkg}}^{\text{VH+dec}}$ . Points with error bars represent the data and stacked histograms represent expected distributions of the signal and background processes. The SM Higgs boson signal with  $m_H = 125$  GeV, denoted as H(125), and the ZZ backgrounds are normalized to the SM expectation, the Z+X background to the estimation from data. The SM Higgs boson signal is separated into two components: the production mode which is targeted by the specific discriminant, and other production modes, where the gluon fusion process dominates.

controlling the contribution of the main SM Higgs boson production modes. The WH and ZH processes are merged into VH. Contributions of the  $b\bar{b}H$  and  $tH$  production modes are also taken into account in the fit. The  $b\bar{b}H$  contribution is floated together with gluon fusion and  $tH$  production mode is floated with  $t\bar{t}H$ .

The results are reported in Fig. 13 (left) and compared to the expected signal-strength modifiers in Table 3.

Table 3: Expected and observed signal-strength modifiers with Run 2 data. The observed uncertainty numbers are broken into statistical (first) and systematic (second) sources.

	Expected	Observed
$\mu_{\text{inclusive}}$	$1.00^{+0.08}_{-0.08}(\text{stat.})^{+0.09}_{-0.07}(\text{syst.})$	$0.94^{+0.07}_{-0.07}(\text{stat.})^{+0.08}_{-0.07}(\text{syst.})$
$\mu_{\text{ggH}}$	$1.00^{+0.10}_{-0.10}(\text{stat.})^{+0.09}_{-0.07}(\text{syst.})$	$0.97^{+0.09}_{-0.09}(\text{stat.})^{+0.09}_{-0.07}(\text{syst.})$
$\mu_{\text{VBF}}$	$1.00^{+0.54}_{-0.45}(\text{stat.})^{+0.27}_{-0.14}(\text{syst.})$	$0.64^{+0.45}_{-0.36}(\text{stat.})^{+0.16}_{-0.09}(\text{syst.})$
$\mu_{\text{VH}}$	$1.00^{+0.91}_{-0.72}(\text{stat.})^{+0.29}_{-0.16}(\text{syst.})$	$1.15^{+0.89}_{-0.72}(\text{stat.})^{+0.26}_{-0.16}(\text{syst.})$
$\mu_{\text{t}\bar{t}H, tH}$	$1.00^{+1.16}_{-0.73}(\text{stat.})^{+0.19}_{-0.04}(\text{syst.})$	$0.13^{+0.92}_{-0.13}(\text{stat.})^{+0.11}_{-0.00}(\text{syst.})$

Two signal-strength modifiers  $\mu_{\text{ggH}, \text{t}\bar{t}H, b\bar{b}H, tH}$  and  $\mu_{\text{VBF}, \text{VH}}$  are introduced as scale factors for the fermion and vector-boson induced contribution to the expected SM cross section. A two-dimensional fit is performed, profiling  $m_H$ , leading to the measurements of  $\mu_{\text{ggH}, \text{t}\bar{t}H, b\bar{b}H, tH} = 0.96^{+0.11}_{-0.12}$  and  $\mu_{\text{VBF}, \text{VH}} = 0.83^{+0.29}_{-0.35}$ .

The 68% and 95% CL contours in the  $(\mu_{\text{ggH}, \text{t}\bar{t}H, b\bar{b}H, tH}, \mu_{\text{VBF}, \text{VH}})$  plane are shown in Fig. 13 (right).

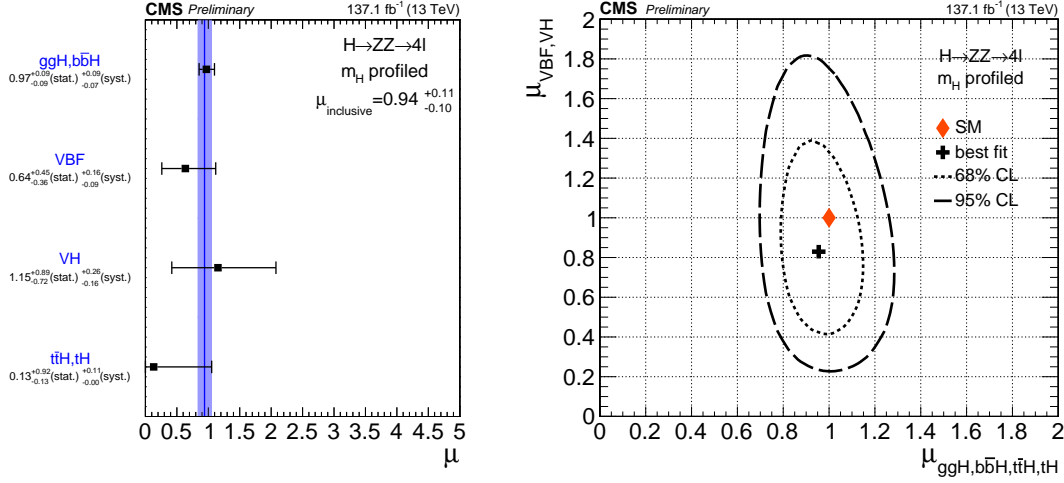


Figure 13: (Left) Results of likelihood scans for the signal-strength modifiers corresponding to the main SM Higgs boson production modes, compared to the combined  $\mu$  shown as a vertical line. The horizontal bars and the filled band indicate the  $\pm 1\sigma$  uncertainties. The uncertainties include both statistical and systematic sources. (Right) Result of the 2D likelihood scan for the  $\mu_{ggH, t\bar{t}H, b\bar{b}H, tH}$  and  $\mu_{VBF, VH}$  signal-strength modifiers. The solid and dashed contours show the 68% and 95% CL regions, respectively. The cross indicates the best-fit value, and the diamond represents the expected value for the SM Higgs boson.

## 10.2 Simplified template cross section

We also present the results for STXS, a measurement strategy detailed in the CERN Yellow Report 4 of the LHC-HXSWG [24]. The Stage 0 Bins correspond to the H boson production mechanisms. The previous Run 2 analysis has reported the measured Stage 0 results [15]. With full Run 2 data, this analysis targets the finer Stage 1.1 Bins. The theoretical uncertainties on the overall signal cross sections are removed, while the theoretical uncertainties which can cause migration of events between the various categories are kept in this measurement.

The measured cross sections, normalized to the SM prediction are shown in Fig. 14 for Stage 0 and in Fig. 15 for Stage 1.1. The correlation matrix for Stage 1.1 is shown in Fig. 16. The dominant experimental sources of systematic uncertainty are the same as in the measurement of the signal strength, while the dominant theoretical source is the uncertainty in the category migration for the  $ggH$  process.

## 10.3 Fiducial cross section

In this section the measurement of the cross section for the production and decay  $pp \rightarrow H \rightarrow 4\ell$  within a fiducial volume defined to match closely the reconstruction level selection is presented. This measurement has minimal dependence on the assumptions of the relative fraction or kinematic distributions of the separate production modes. The definition of the fiducial volume is very similar to the definition used in Ref. [21]. The differences with respect to Ref. [21] are that leptons are defined as “dressed” leptons, as opposed to produced bare leptons, and the lepton isolation criteria is updated to match the reconstruction level selection. Leptons are “dressed” by adding the four-momenta of photons within  $\Delta R < 0.3$  to the bare leptons, and leptons are considered isolated if the sum of scalar  $p_T$  of all stable particles within  $\Delta R < 0.3$  from the lepton is less than  $0.35 \cdot p_T$ . In order to reduce the experimental uncertainties, jets with  $p_T > 30 \text{ GeV}$  and  $|\eta| < 2.5$  are considered for the differential cross sections related to jet ob-

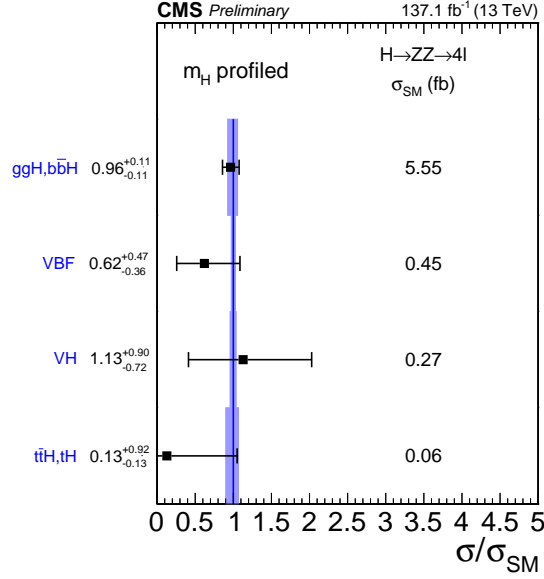


Figure 14: The ratios between measured cross sections and the SM prediction for Stage 0 Bins with  $m_H$  profiled in the fit. The band around the vertical band shows the theoretical uncertainties on the SM cross section predictions for each Stage 0 Bin. Cross section values are reported for the best fit mass value  $m_H = 125.1$  GeV.

servables. An increase in model dependence compared to Ref. [21] is observed when using the ZZ candidate selection at reconstruction level where the candidate with the best  $\mathcal{D}_{\text{bkg}}^{\text{kin}}$  discriminant value is chosen. Therefore the fiducial cross section measurement is performed using the event selection algorithm in Ref. [21]. Specifically the  $Z_1$  candidate is chosen to be the one with  $m(Z_1)$  closest to the nominal Z boson mass, and in cases where multiple  $Z_2$  candidates satisfy all criteria, the pair of leptons with the largest sum of the transverse momenta magnitudes is chosen. The full fiducial volume definition is detailed in Table 4 and the acceptance for various SM production modes is given in Table 5.

Table 4: Summary of requirements used in the definition of the fiducial phase space for the  $H \rightarrow 4\ell$  cross section measurements.

Requirements for the $H \rightarrow 4\ell$ fiducial phase space	
Lepton kinematics and isolation	
Leading lepton $p_T$	$p_T > 20$ GeV
Next-to-leading lepton $p_T$	$p_T > 10$ GeV
Additional electrons (muons) $p_T$	$p_T > 7(5)$ GeV
Pseudorapidity of electrons (muons)	$ \eta  < 2.5(2.4)$
Sum of scalar $p_T$ of all stable particles within $\Delta R < 0.3$ from lepton	$< 0.35 \cdot p_T$
Event topology	
Existence of at least two same-flavor OS lepton pairs, where leptons satisfy criteria above	
Inv. mass of the $Z_1$ candidate	$40 \text{ GeV} < m_{Z_1} < 120 \text{ GeV}$
Inv. mass of the $Z_2$ candidate	$12 \text{ GeV} < m_{Z_2} < 120 \text{ GeV}$
Distance between selected four leptons	$\Delta R(\ell_i, \ell_j) > 0.02$ for any $i \neq j$
Inv. mass of any opposite sign lepton pair	$m_{\ell^+ \ell^-} > 4 \text{ GeV}$
Inv. mass of the selected four leptons	$105 \text{ GeV} < m_{4\ell} < 140 \text{ GeV}$

A maximum likelihood fit of the signal and background parameterizations to the observed  $4\ell$



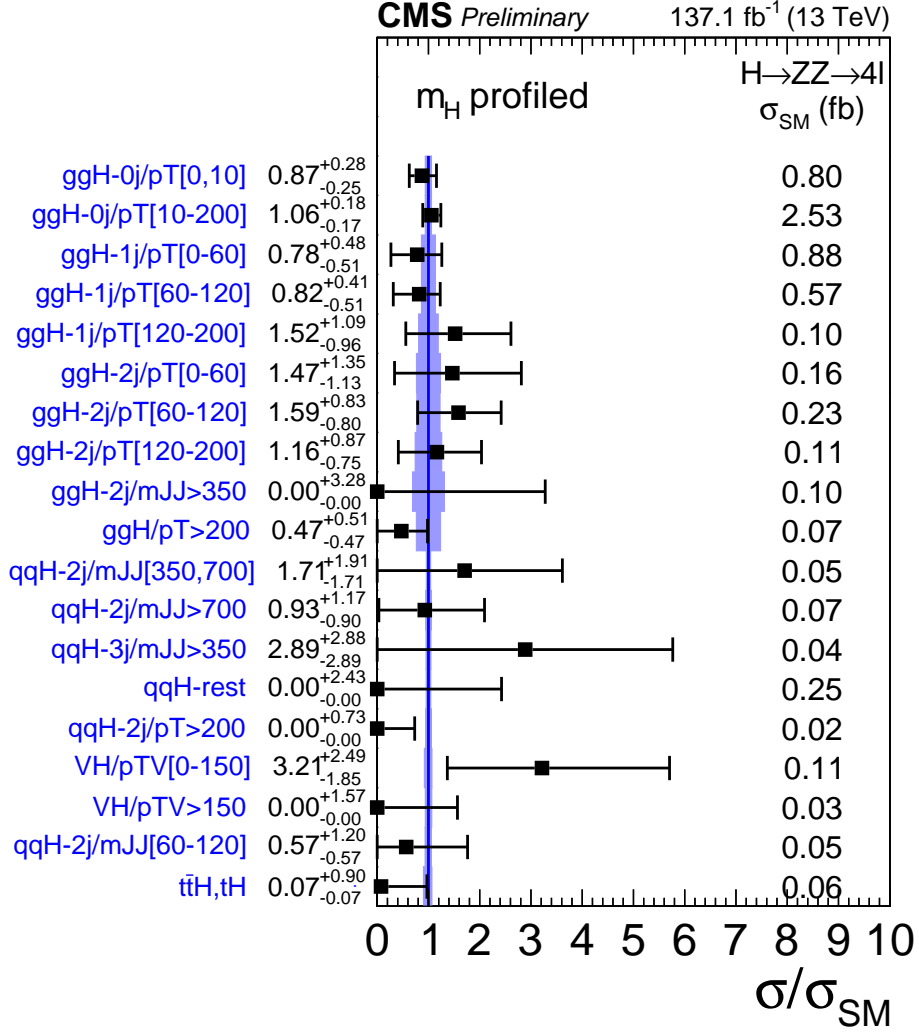


Figure 15: The ratios between measured cross sections and the SM prediction for Stage 1.1 Bins with  $m_H$  profiled in the fit. The band around the vertical band shows the theoretical uncertainties on the SM cross section predictions for each Stage 1.1 Bin. The cross section ratios are constrained to be non-negative. The parameters whose best-fit values are at zero are known to have 68% CL intervals which slightly under-cover. Cross section values are reported for the best fit mass value  $m_H = 125.1$  GeV.

mass distribution,  $N_{\text{obs}}(m_{4\ell})$ , is performed to extract the integrated fiducial cross section for  $pp \rightarrow H \rightarrow 4\ell$  ( $\sigma_{\text{fid}}$ ). The fit is done inclusive (i.e. without any event categorization) and does not use the  $\mathcal{D}_{\text{bkg}}^{\text{kin}}$  observable in order to minimize the model dependence. The fit is performed simultaneously in all final states and assumes a H boson mass of  $m_H = 125.09$  GeV, and the branching fraction of the H boson to different final states ( $4e, 4\mu, 2e2\mu$ ) is allowed to float. Systematic uncertainties are included in the form of nuisance parameters and the results are obtained using an asymptotic approach [69] with a test statistic based on the profile likelihood ratio [70]. This procedure accounts for the unfolding of detector effects from the observed distributions and is the same as in Refs. [21] and [71].

The number of expected events in each final state  $f$  and in each bin  $i$  of a considered observable is expressed as a function of  $m_{4\ell}$  as:



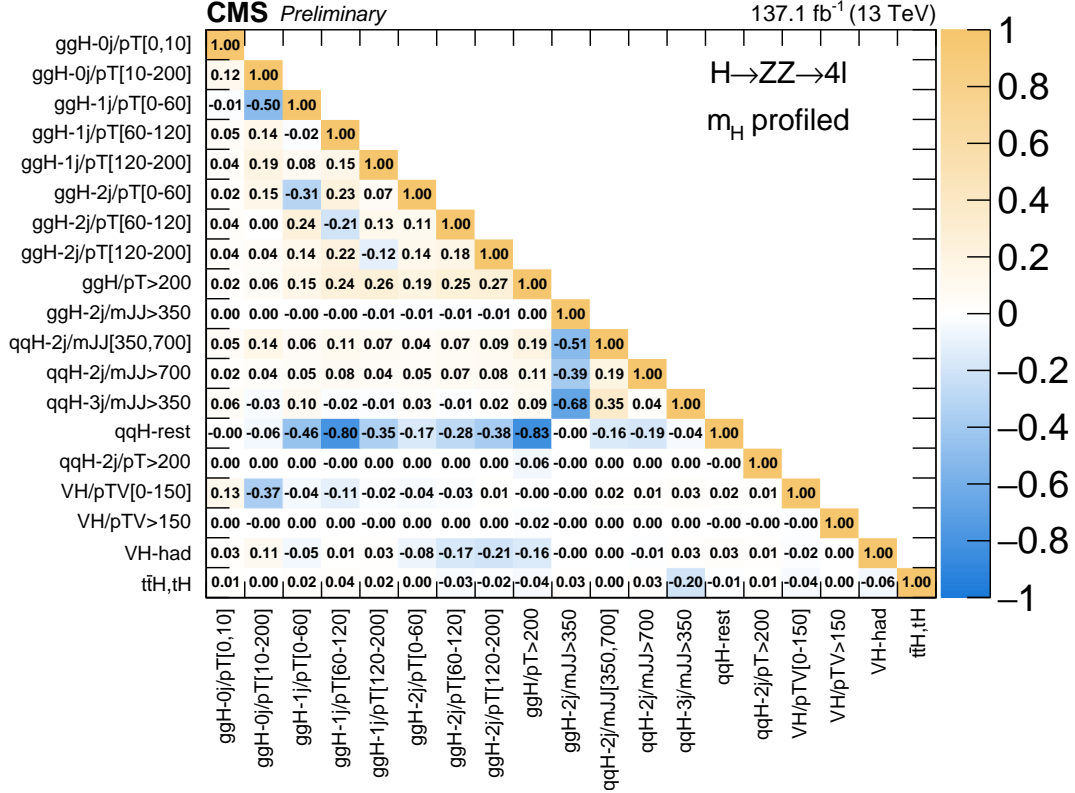


Figure 16: Correlation matrix of the fitted signal strengths for Stage 1.1 Bins.

$$\begin{aligned}
 N_{\text{obs}}^{f,i}(m_{4\ell}) &= N_{\text{fid}}^{f,i}(m_{4\ell}) + N_{\text{nonfid}}^{f,i}(m_{4\ell}) + N_{\text{nonres}}^{f,i}(m_{4\ell}) + N_{\text{bkg}}^{f,i}(m_{4\ell}) \\
 &= \epsilon_{i,j}^f \cdot \left(1 + f_{\text{nonfid}}^{f,i}\right) \cdot \sigma_{\text{fid}}^{f,j} \cdot \mathcal{L} \cdot \mathcal{P}_{\text{res}}(m_{4\ell}) \\
 &\quad + N_{\text{nonres}}^{f,i} \cdot \mathcal{P}_{\text{nonres}}(m_{4\ell}) + N_{\text{bkg}}^{f,i} \cdot \mathcal{P}_{\text{bkg}}(m_{4\ell}),
 \end{aligned} \tag{6}$$

The shape of the resonant signal contribution,  $\mathcal{P}_{\text{res}}(m_{4\ell})$ , is described by a double-sided Crystal Ball function as described in Section 8, and the normalization is proportional to the fiducial cross section. The shape of the non-resonant signal contribution,  $\mathcal{P}_{\text{nonres}}(m_{4\ell})$ , which arises from WH, ZH, and  $t\bar{t}H$  production where one of the leptons from the H boson decay is lost or not selected, is modeled by a Landau distribution whose shape parameters are constrained in the fit to be within a range determined from simulation. This contribution is referred to as the “combinatorial signal” and is treated as a background in this measurement.

The  $\epsilon_{i,j}^f$  represents the detector response matrix that maps the number of expected events in a given observable bin  $j$  at the fiducial level to the number of expected events in the bin  $i$  at the reconstruction level. This response matrix is measured using signal simulation samples and corrected for residual differences between data and simulation. In the case of the integrated fiducial cross section measurement the efficiencies reduce to a single values, which for different SM signal models are listed in Table 5.

An additional resonant contribution arises from events which are accepted but do not originate from the fiducial phase space. These events are due to detector effects which cause differences between the quantities used for the fiducial phase space definition and the analogous quantities

at the reconstruction level. This contribution is treated as background and is referred to as the “non-fiducial signal” contribution. The shape of these events is verified using simulation to be identical to the shape of the fiducial signal, and its normalization is fixed to be a fraction of the fiducial signal component. The value of this fraction, which we denote as  $f_{\text{nonfid}}$ , has been determined from simulation for each of the studied signal models. The value of  $f_{\text{nonfid}}$  for different signal models is shown in Table 5.

Table 5: Summary of different SM signal models. For all production modes the values given are for  $m_H = 125$  GeV. The uncertainties listed are statistical only, and the statistical uncertainty on the acceptance is  $\sim 0.001$ .

Signal process	$\mathcal{A}_{\text{fid}}$	$\epsilon$	$f_{\text{nonfid}}$	$(1 + f_{\text{nonfid}})\epsilon$
Individual Higgs boson production modes				
gg→H (POWHEG)	$0.402 \pm 0.001$	$0.592 \pm 0.002$	$0.053 \pm 0.001$	$0.624 \pm 0.002$
VBF (POWHEG)	$0.444 \pm 0.002$	$0.605 \pm 0.003$	$0.043 \pm 0.001$	$0.631 \pm 0.003$
WH (POWHEG+MINLO)	$0.325 \pm 0.002$	$0.588 \pm 0.003$	$0.075 \pm 0.002$	$0.632 \pm 0.004$
ZH (POWHEG+MINLO)	$0.340 \pm 0.003$	$0.594 \pm 0.005$	$0.081 \pm 0.004$	$0.643 \pm 0.006$
ttH (POWHEG)	$0.314 \pm 0.003$	$0.585 \pm 0.006$	$0.169 \pm 0.006$	$0.684 \pm 0.007$

The integrated fiducial cross section is measured to be  $\sigma_{\text{fid.}} = 2.73^{+0.30}_{-0.29} = 2.73^{+0.23}_{-0.22}(\text{stat.})^{+0.24}_{-0.19}(\text{syst.})$  fb at  $m_H = 125.09$  GeV. This can be compared to the SM expectation  $\sigma_{\text{fid.}}^{\text{SM}} = 2.76 \pm 0.14$  fb. The integrated fiducial cross section as a function of center-of-mass energy is also shown in Fig. 17. The measured differential cross section results for  $p_T(\text{H})$ ,  $|y(\text{H})|$ ,  $N(\text{jets})$ , and  $p_T(\text{jet})$  can also be seen in Fig. 17. The dominant sources of systematic uncertainty are the experimental uncertainties in the lepton identification efficiencies and luminosity measurement, and the theoretical sources of uncertainty are found to be subdominant. In order to assess the model dependence of the measurement, the unfolding procedure is repeated using different response matrices created by varying the relative fraction of each SM production mode within its experimental constraints. The uncertainty is determined to be negligible with respect to the experimental systematic uncertainties.

## 11 Summary

Several measurements of Higgs (H) boson production in the four-lepton final state at  $\sqrt{s} = 13$  TeV have been presented, using data samples corresponding to an integrated luminosity of  $137.1 \text{ fb}^{-1}$ . The measured signal-strength modifier is  $\mu = 0.94^{+0.07}_{-0.07}(\text{stat.})^{+0.08}_{-0.07}(\text{syst.})$  and integrated fiducial cross section is measured to be  $\sigma_{\text{fid.}} = 2.73^{+0.23}_{-0.22}(\text{stat.})^{+0.24}_{-0.19}(\text{syst.})$  fb. The signal-strength modifiers for the main H boson production modes are also constrained. Measurements of the simplified template cross sections, designed to quantify the different H boson production processes in specific regions of phase space, have been measured for the first time with the Stage 1.1 recommendation. Differential cross sections as a function of the  $p_T$  and rapidity of the H boson, the number of associated jets, and the  $p_T$  of the leading associated jet are determined. All results are consistent, within their uncertainties, with the expectations for the Standard Model H boson.

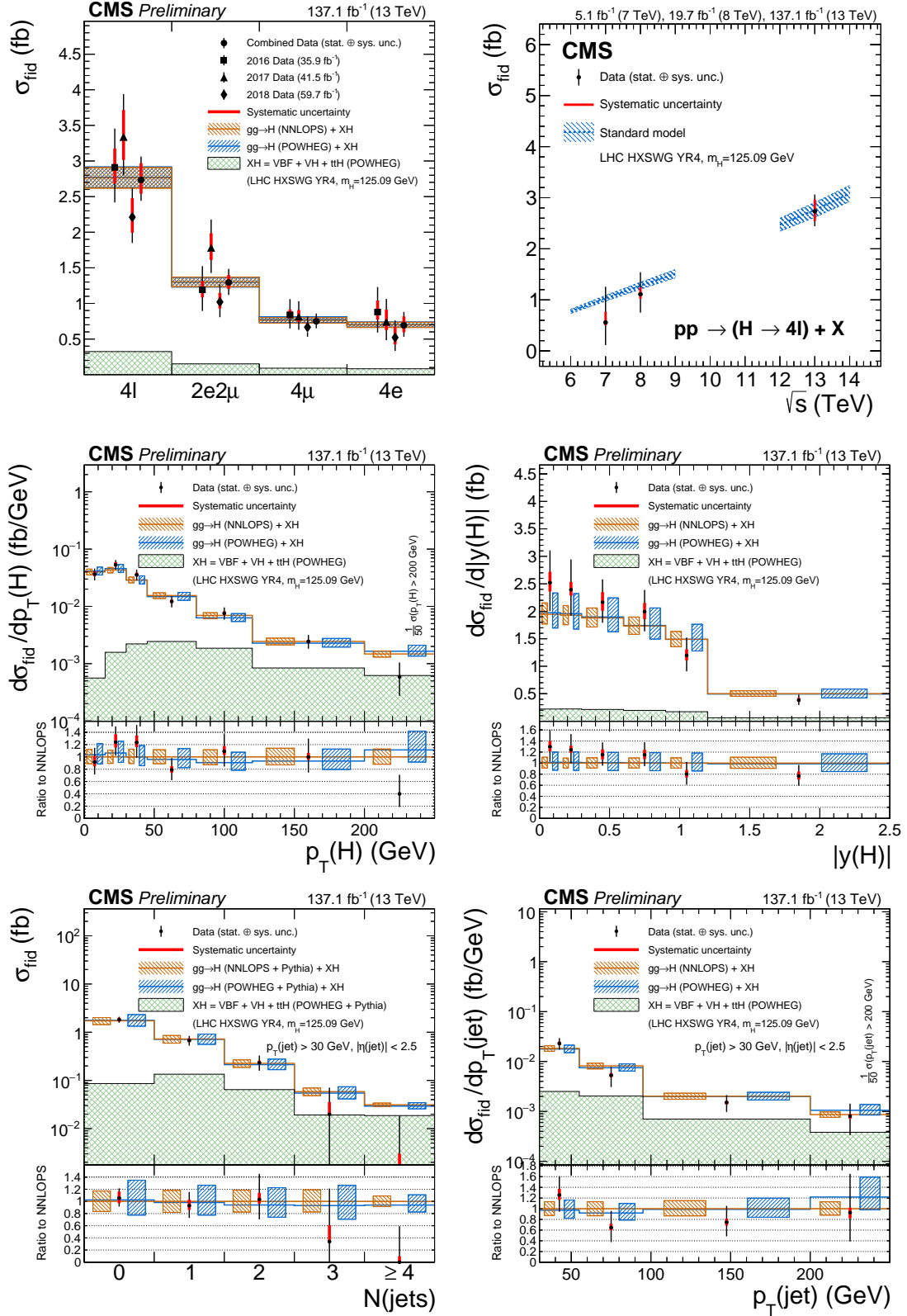


Figure 17: The measured inclusive fiducial cross section in different final states (top left). The measured fiducial cross section as a function of  $\sqrt{s}$  (top right). The acceptance is calculated using POWHEG at  $\sqrt{s}=13$  TeV and HRES [63, 65] at  $\sqrt{s}=7$  and 8 TeV and the total gluon fusion cross section and uncertainty are taken from Ref. [32]. The fiducial volume for  $\sqrt{s}=6-9$  TeV uses the lepton isolation definition from Ref. [21], while for  $\sqrt{s}=12-14$  TeV the definition described in the text is used. The results of the differential cross section measurement for  $p_T(H)$  (middle left),  $|y(H)|$  (middle right) and  $N(\text{jets})$  (bottom left),  $p_T$  of the leading jet (bottom right). The acceptance and theoretical uncertainties in the differential bins are calculated using POWHEG. The sub-dominant component of the the signal (VBF + VH + ttH) is denoted as XH.

## References

- [1] CMS Collaboration, “Observation of a new boson at a mass of 125 GeV with the CMS experiment at the LHC”, *Phys. Lett. B* **716** (2012) 30, doi:10.1016/j.physletb.2012.08.021, arXiv:1207.7235.
- [2] ATLAS Collaboration, “Observation of a new particle in the search for the Standard Model Higgs boson with the ATLAS detector at the LHC”, *Phys. Lett. B* **716** (2012) 1, doi:10.1016/j.physletb.2012.08.020, arXiv:1207.7214.
- [3] F. Englert and R. Brout, “Broken Symmetry and the Mass of Gauge Vector Mesons”, *Phys. Rev. Lett.* **13** (1964) 321, doi:10.1103/PhysRevLett.13.321.
- [4] P. W. Higgs, “Broken symmetries, massless particles and gauge fields”, *Phys. Lett.* **12** (1964) 132, doi:10.1016/0031-9163(64)91136-9.
- [5] P. W. Higgs, “Broken Symmetries and the Masses of Gauge Bosons”, *Phys. Rev. Lett.* **13** (1964) 508, doi:10.1103/PhysRevLett.13.508.
- [6] G. Guralnik, C. Hagen, and T. Kibble, “Global Conservation Laws and Massless Particles”, *Phys. Rev. Lett.* **13** (1964) 585, doi:10.1103/PhysRevLett.13.585.
- [7] P. W. Higgs, “Spontaneous Symmetry Breakdown without Massless Bosons”, *Phys. Rev.* **145** (1966) 1156, doi:10.1103/PhysRev.145.1156.
- [8] T. Kibble, “Symmetry breaking in nonAbelian gauge theories”, *Phys. Rev.* **155** (1967) 1554, doi:10.1103/PhysRev.155.1554.
- [9] CMS Collaboration, “Precise determination of the mass of the Higgs boson and tests of compatibility of its couplings with the standard model predictions using proton collisions at 7 and 8 TeV”, *Eur. Phys. J. C* **75** (2015) 212, doi:10.1140/epjc/s10052-015-3351-7, arXiv:1412.8662.
- [10] ATLAS Collaboration, “Measurements of the Higgs boson production and decay rates and coupling strengths using  $pp$  collision data at  $\sqrt{s} = 7$  and 8 TeV in the ATLAS experiment”, *Eur. Phys. J. C* **76** (2016) doi:10.1140/epjc/s10052-015-3769-y, arXiv:1507.04548.
- [11] ATLAS and CMS Collaborations, “Combined Measurement of the Higgs Boson Mass in  $pp$  Collisions at  $\sqrt{s} = 7$  and 8 TeV with the ATLAS and CMS Experiments”, *Phys. Rev. Lett.* **114** (2015) 191803, doi:10.1103/PhysRevLett.114.191803, arXiv:1503.07589.
- [12] ATLAS and CMS Collaborations, “Measurements of the Higgs boson production and decay rates and constraints on its couplings from a combined ATLAS and CMS analysis of the LHC  $pp$  collision data at  $\sqrt{s} = 7$  and 8 TeV”, *JHEP* **08** (2016) 45, doi:10.1007/JHEP08(2016)045, arXiv:1606.02266.
- [13] CMS Collaboration, “Combined measurements of the Higgs boson’s couplings at  $\sqrt{s} = 13$  TeV”, CMS Physics Analysis Summary CMS-PAS-HIG-17-031, 2018.
- [14] CMS Collaboration, “Measurements of properties of the Higgs boson decaying into the four-lepton final state in  $pp$  collisions at  $\sqrt{s} = 13$  TeV”, *JHEP* **11** (2017) 047, doi:10.1007/JHEP11(2017)047, arXiv:1706.09936.

- [15] CMS Collaboration, “Measurements of properties of the Higgs boson in the four-lepton final state at  $\sqrt{s} = 13$  TeV”, CMS-PAS-HIG 18-001, 2018.
- [16] CMS Collaboration, “Measurement of the properties of a Higgs boson in the four-lepton final state”, *Phys. Rev. D* **89** (2014) 092007, doi:10.1103/PhysRevD.89.092007, arXiv:1312.5353.
- [17] CMS Collaboration, “Study of the Mass and Spin-Parity of the Higgs Boson Candidate via Its Decays to Z Boson Pairs”, *Phys. Rev. Lett.* **110** (2013) 081803, doi:10.1103/PhysRevLett.110.081803, arXiv:1212.6639.
- [18] CMS Collaboration, “Constraints on the spin-parity and anomalous HVV couplings of the Higgs boson in proton collisions at 7 and 8 TeV”, *Phys. Rev. D* **92** (2015) 012004, doi:10.1103/PhysRevD.92.012004, arXiv:1411.3441.
- [19] CMS Collaboration, “Constraints on the Higgs boson width from off-shell production and decay to Z-boson pairs”, *Phys. Lett. B* **736** (2014) 64, doi:10.1016/j.physletb.2014.06.077, arXiv:1405.3455.
- [20] CMS Collaboration, “Limits on the Higgs boson lifetime and width from its decay to four charged leptons”, *Phys. Rev. D* **92** (2015) 072010, doi:10.1103/PhysRevD.92.072010, arXiv:1507.06656.
- [21] CMS Collaboration, “Measurement of differential and integrated fiducial cross sections for Higgs boson production in the four-lepton decay channel in pp collisions at  $\sqrt{s} = 7$  and 8 TeV”, *JHEP* **04** (2016) 005, doi:10.1007/JHEP04(2016)005, arXiv:1512.08377.
- [22] CMS Collaboration, “Constraints on anomalous Higgs boson couplings using production and decay information in the four-lepton final state”, *Phys. Lett. B* **775** (2017) 1–24, doi:10.1016/j.physletb.2017.10.021, arXiv:1707.00541.
- [23] CMS Collaboration, “Measurements of the Higgs boson width and anomalous HVV couplings from on-shell and off-shell production in the four-lepton final state”, arXiv:1901.00174.
- [24] LHC Higgs Cross Section Working Group, “Handbook of LHC Higgs Cross Sections: 4. Deciphering the Nature of the Higgs Sector”, CERN-2017-002-M (CERN, Geneva, 2016) arXiv:1610.07922.
- [25] LHCXSWG, “Simplified template cross section, stage 1.1”, LHCXSWG Twiki (2018).
- [26] A. Dominguez et al., “CMS Technical Design Report for the Pixel Detector Upgrade”, Technical Report CERN-LHCC-2012-016. CMS-TDR-11, Sep, 2012. doi:10.2172/1151650.
- [27] CMS Collaboration, “The CMS experiment at the CERN LHC”, *JINST* **3** (2008) S08004, doi:10.1088/1748-0221/3/08/S08004.
- [28] S. Alioli, P. Nason, C. Oleari, and E. Re, “NLO vector-boson production matched with shower in POWHEG”, *JHEP* **07** (2008) 060, doi:10.1088/1126-6708/2008/07/060, arXiv:0805.4802.

- 
- [29] P. Nason, “A new method for combining NLO QCD with shower Monte Carlo algorithms”, *JHEP* **11** (2004) 040, doi:10.1088/1126-6708/2004/11/040, arXiv:hep-ph/0409146.
- [30] S. Frixione, P. Nason, and C. Oleari, “Matching NLO QCD computations with parton shower simulations: the POWHEG method”, *JHEP* **11** (2007) 070, doi:10.1088/1126-6708/2007/11/070, arXiv:0709.2092.
- [31] G. Luisoni, P. Nason, C. Oleari, and F. Tramontano, “ $HW^\pm/HZ + 0$  and 1 jet at NLO with the POWHEG BOX interfaced to GoSam and their merging within MiNLO”, *JHEP* **10** (2013) 1, doi:10.1007/JHEP10(2013)083, arXiv:1306.2542.
- [32] C. Anastasiou et al., “High precision determination of the gluon fusion Higgs boson cross-section at the LHC”, *JHEP* **2016** (2016), no. 5, 1, doi:10.1007/JHEP05(2016)058, arXiv:1602.00695.
- [33] Y. Gao et al., “Spin determination of single-produced resonances at hadron colliders”, *Phys. Rev. D* **81** (2010) 075022, doi:10.1103/PhysRevD.81.075022, arXiv:1001.3396. [Erratum: doi:10.1103/PhysRevD.81.079905].
- [34] S. Bolognesi et al., “On the spin and parity of a single-produced resonance at the LHC”, *Phys. Rev. D* **86** (2012) 095031, doi:10.1103/PhysRevD.86.095031, arXiv:1208.4018.
- [35] I. Anderson et al., “Constraining anomalous  $HVV$  interactions at proton and lepton colliders”, *Phys. Rev. D* **89** (2014) 035007, doi:10.1103/PhysRevD.89.035007, arXiv:1309.4819.
- [36] A. V. Gritsan, R. Roentsch, M. Schulze, and M. Xiao, “Constraining anomalous Higgs boson couplings to the heavy flavor fermions using matrix element techniques”, *Phys. Rev. D* **94** (2016), no. 5, 055023, doi:10.1103/PhysRevD.94.055023, arXiv:1606.03107.
- [37] J. M. Campbell and R. K. Ellis, “MCFM for the Tevatron and the LHC”, *Nucl. Phys. Proc. Suppl.* **205** (2010) 10, doi:10.1016/j.nuclphysbps.2010.08.011, arXiv:1007.3492.
- [38] NNPDF Collaboration, “Parton distributions from high-precision collider data”, *Eur. Phys. J. C* **77** (2017) 663, doi:10.1140/epjc/s10052-017-5199-5, arXiv:1706.00428.
- [39] T. Sjöstrand et al., “An introduction to pythia 8.2”, *Computer Physics Communications* **191** (2015) 159, doi:10.1016/j.cpc.2015.01.024.
- [40] CMS Collaboration, “Event generator tunes obtained from underlying event and multiparton scattering measurements”, *Eur. Phys. J. C* **76** (2016) 155, doi:10.1140/epjc/s10052-016-3988-x, arXiv:1512.00815.
- [41] GEANT4 Collaboration, “GEANT4: a simulation toolkit”, *Nucl. Instrum. Meth. A* **506** (2003) 250, doi:10.1016/S0168-9002(03)01368-8.
- [42] J. Allison et al., “Geant4 developments and applications”, *IEEE Trans. Nucl. Sci.* **53** (2006) 270, doi:10.1109/TNS.2006.869826.

- [43] CMS Collaboration, “Particle-flow reconstruction and global event description with the cms detector”, *JINST* **12** (2017) P10003, doi:10.1088/1748-0221/12/10/P10003, arXiv:1706.04965.
- [44] CMS Collaboration, “Performance of CMS muon reconstruction in  $pp$  collision events at  $\sqrt{s} = 7$  TeV”, *JINST* **7** (2012) P10002, doi:10.1088/1748-0221/7/10/P10002, arXiv:1206.4071.
- [45] CMS Collaboration, “Performance of electron reconstruction and selection with the CMS detector in proton-proton collisions at  $\sqrt{s} = 8$  TeV”, *JINST* **10** (2015) P06005, doi:10.1088/1748-0221/10/06/P06005, arXiv:1502.02701.
- [46] CMS Collaboration, “Electron and Photon performance in CMS with the full 2017 data sample and additional highlights for the CALOR 2018 conference”, CMS Detector Performance Summary CMS-DPS-2018/2017, 2018.
- [47] T. Chen and C. Guestrin, “XGBoost: A Scalable Tree Boosting System”, doi:10.1145/2939672.2939785, arXiv:1603.02754.
- [48] M. Cacciari, G. P. Salam, and G. Soyez, “The anti- $k_t$  jet clustering algorithm”, *JHEP* **04** (2008) 063, doi:10.1088/1126-6708/2008/04/063, arXiv:0802.1189.
- [49] M. Cacciari, G. P. Salam, and G. Soyez, “FastJet user manual”, *Eur. Phys. J. C* **72** (2012) 1896, doi:10.1140/epjc/s10052-012-1896-2, arXiv:1111.6097.
- [50] CMS Collaboration, “Jet energy scale and resolution in the CMS experiment in  $pp$  collisions at 8 TeV”, *JINST* **12** (2017), no. 02, P02014, doi:10.1088/1748-0221/12/02/P02014, arXiv:1607.03663.
- [51] CMS Collaboration, “Jet algorithms performance in 13 TeV data”, CMS Physics Analysis Summary CMS-PAS-JME-16-003, 2016.
- [52] CMS Collaboration, “Identification of heavy-flavour jets with the CMS detector in  $pp$  collisions at 13 TeV”, *JINST* **13** (2018), no. 05, P05011, doi:10.1088/1748-0221/13/05/P05011, arXiv:1712.07158.
- [53] Particle Data Group Collaboration, “Review of Particle Physics”, *Chin. Phys. C* **40** (2016), no. 10, 100001, doi:10.1088/1674-1137/40/10/100001.
- [54] CMS Collaboration, “Search for a Higgs Boson in the Mass Range from 145 to 1000 GeV Decaying to a Pair of W or Z Bosons”, *JHEP* **10** (2015) 144, doi:10.1007/JHEP10(2015)144, arXiv:1504.00936.
- [55] M. Grazzini, S. Kallweit, and D. Rathlev, “ZZ production at the LHC: Fiducial cross sections and distributions in NNLO QCD”, *Phys. Lett. B* **750** (2015) 407 – 410, doi:10.1016/j.physletb.2015.09.055, arXiv:1507.06257.
- [56] A. Bierweiler, T. Kasprzik, and J. H. Kuhn, “Vector-boson pair production at the LHC to  $\mathcal{O}(\alpha^3)$  accuracy”, *JHEP* **12** (2013) 071, doi:10.1007/JHEP12(2013)071, arXiv:1305.5402.
- [57] M. Bonvini et al., “Signal-background interference effects in  $gg \rightarrow H \rightarrow WW$  beyond leading order”, *Phys. Rev. D* **88** (2013) 034032, doi:10.1103/PhysRevD.88.034032, arXiv:1304.3053.

- 
- [58] K. Melnikov and M. Dowling, “Production of two Z-bosons in gluon fusion in the heavy top quark approximation”, *Phys. Lett. B* **744** (2015) 43, doi:10.1016/j.physletb.2015.03.030, arXiv:1503.01274.
  - [59] C. S. Li, H. T. Li, D. Y. Shao, and J. Wang, “Soft gluon resummation in the signal-background interference process of  $gg(\rightarrow h^*) \rightarrow ZZ$ ”, (2015). arXiv:1504.02388.
  - [60] G. Passarino, “Higgs CAT”, *Eur. Phys. J. C* **74** (2014) 2866, doi:10.1140/epjc/s10052-014-2866-7, arXiv:1312.2397.
  - [61] S. Catani and M. Grazzini, “An NNLO subtraction formalism in hadron collisions and its application to Higgs boson production at the LHC”, *Phys. Rev. Lett.* **98** (2007) 222002, doi:10.1103/PhysRevLett.98.222002, arXiv:hep-ph/0703012.
  - [62] M. Grazzini, “NNLO predictions for the Higgs boson signal in the  $H \rightarrow WW \rightarrow \ell\nu\ell\nu$  and  $H \rightarrow ZZ \rightarrow 4\ell$  decay channels”, *JHEP* **02** (2008) 043, doi:10.1088/1126-6708/2008/02/043, arXiv:0801.3232.
  - [63] M. Grazzini and H. Sargsyan, “Heavy-quark mass effects in Higgs boson production at the LHC”, *JHEP* **09** (2013) 129, doi:10.1007/JHEP09(2013)129, arXiv:1306.4581.
  - [64] L. Landau, “On the energy loss of fast particles by ionization”, *J. Phys. (USSR)* **8** (1944) 201.
  - [65] D. de Florian, G. Ferrera, M. Grazzini, and D. Tommasini, “Higgs boson production at the LHC: transverse momentum resummation effects in the  $H \rightarrow \gamma\gamma$ ,  $H \rightarrow WW \rightarrow \ell\nu\ell\nu$  and  $H \rightarrow ZZ \rightarrow 4\ell$  decay modes”, *JHEP* **06** (2012) 132, doi:10.1007/JHEP06(2012)132, arXiv:1203.6321.
  - [66] E. Bagnaschi, G. Degrossi, P. Slavich, and A. Vicini, “Higgs production via gluon fusion in the POWHEG approach in the SM and in the MSSM”, *JHEP* **02** (2012) 088, doi:10.1007/JHEP02(2012)088, arXiv:1111.2854.
  - [67] K. Hamilton, P. Nason, E. Re, and G. Zanderighi, “NNLOPS simulation of Higgs boson production”, *JHEP* **10** (2013) 222, doi:10.1007/JHEP10(2013)222, arXiv:1309.0017.
  - [68] F. Garwood, “Fiducial Limits for the Poisson Distribution”, *Biometrika* **28** (1936), no. 3-4, 437, doi:10.1093/biomet/28.3-4.437.
  - [69] ATLAS and CMS Collaborations, LHC Higgs Combination Group, “Procedure for the LHC Higgs boson search combination in summer 2011”, ATL-PHYS-PUB/CMS NOTE 2011-11, 2011/005, CERN, 2011.
  - [70] G. Cowan, K. Cranmer, E. Gross, and O. Vitells, “Asymptotic formulae for likelihood-based tests of new physics”, *Eur. Phys. J. C* **71** (2011) 1554, doi:10.1140/epjc/s10052-011-1554-0, 10.1140/epjc/s10052-013-2501-z, arXiv:1007.1727.
  - [71] CMS Collaboration, “Measurement of differential cross sections for Higgs boson production in the diphoton decay channel in pp collisions at  $\sqrt{s}=8$  TeV”, *Eur. Phys. J. C* **76** (2015) 13, doi:10.1140/epjc/s10052-015-3853-3, arXiv:1508.07819.